
Article:
Narciso, C., Wu, Q., Brodskiy, P. et al. (4 more authors) (2015) Patterning of wound-induced intercellular Ca2+ flashes in a developing epithelium. Physical Biology new, 12 (5). 056005. ISSN 1478-3967

https://doi.org/10.1088/1478-3975/12/5/056005

Patterning of Wound-Induced Intercellular Ca^{2+} Flashes in a Developing Epithelium

Cody Narciso[1], Qinfeng Wu[1], Pavel Brodskiy[1], George Garston[2], Ruth Baker[2], Alexander Fletcher[2,#] and Jeremiah Zartman[1,#]

Correspondence:
jzartman@nd.edu
alexander.fletcher@maths.ox.ac.uk

[1]Department of Chemical and Biomolecular Engineering, University of Notre Dame, 182 Fitzpatrick Hall, Notre Dame, IN 46556, USA
[2]Wolfson Centre for Mathematical Biology, Mathematical Institute, University of Oxford, Andrew Wiles Building, Radcliffe Observatory Quarter, Woodstock Road, Oxford, OX2 6GG, UK

Short Running Title
Intercellular Ca^{2+} dynamics in a developing epithelium

Keywords
Calcium signaling, Drosophila wing disc, gap junctions, wound healing, computational modeling, homeostasis

ABSTRACT
Differential mechanical force distributions are increasingly recognized to provide important feedback into the control of an organ's final size and shape. As a second messenger that integrates and relays mechanical information to the cell, calcium ions (Ca^{2+}) are a prime candidate for providing important information on both the overall mechanical state of the tissue and resulting behavior at the individual-cell level during development. Still, how the spatiotemporal properties of Ca^{2+} transients reflect the underlying mechanical characteristics of tissues is still poorly understood. Here we use an established model system of an epithelial tissue, the Drosophila wing imaginal disc, to investigate how tissue properties impact the propagation of Ca^{2+} transients induced by laser ablation. The resulting intercellular Ca^{2+} flash is found to be mediated by inositol 1,4,5-trisphosphate (IP_3) and depends on gap junction communication. Further, we find that intercellular Ca^{2+} transients show spatially non-uniform characteristics across the proximal-distal (PD) axis of the larval wing imaginal disc, which exhibit a gradient in cell size and anisotropy. A computational model of $Ca2^{+}$ transients is employed to identify the principle factors explaining the spatiotemporal patterning dynamics of intercellular Ca^{2+} flashes. The relative Ca^{2+} flash anisotropy is principally explained by local cell shape anisotropy. Further, Ca^{2+} velocities are relatively uniform throughout the wing disc, irrespective of cell size or anisotropy. This can be explained by the opposing effects of cell diameter and cell elongation on intercellular Ca^{2+} propagation. Thus, intercellular Ca^{2+} transients follow lines of mechanical tension at velocities that are largely independent of tissue heterogeneity and reflect the mechanical state of the underlying tissue.

1. INTRODUCTION

Calcium (Ca^{2+}) is a universal second messenger that integrates multiple signal inputs to coordinate downstream processes such as control of the cell cycle, apoptosis [1,2], cell migration [3], wound healing [4,5], gene expression [6] and differentiation state during development [7]. Although previous reports have highlighted the complex spatiotemporal dynamics in Ca^{2+} signaling in a variety of contexts, the information encoded in these dynamic responses remains largely undeciphered [3,8]. This is of particular importance in the case of developing epithelia, where it is increasingly recognized that biomechanical signaling, which is mediated in part by Ca^{2+} signaling [9–15], influences tissue morphogenesis and growth regulation [16–19].

An important first step towards understanding the role of Ca^{2+} signaling in organogenesis is to develop a more rigorous characterization of the dynamics of intercellular Ca^{2+} signaling. With the introduction and optimization of GCaMP6, a genetically encoded Ca^{2+} indicator (GECI), Drosophila has emerged as an important and genetically accessible model system to study Ca^{2+} signaling dynamics in epithelia [20–23]. After tissue wounding, a dramatic increase in cytoplasmic Ca^{2+} levels within cells surrounding the wound is observed [24–27]. In the Drosophila embryo, Ca^{2+} has been found to play a critical role in coordinating the wound inflammatory response through DUOX activation and subsequent release of hydrogen peroxide after wounding by laser ablation [26]. The rapid response (or 'flash') and decay of Ca^{2+} in the cells surrounding a wound correlates with waves of actomyosin and cell constriction that flow back towards the location of the wound's edge and later contribute to the formation of an actomyosin cable that drives wound closure [24]. Studies in the pupal thorax have shown that even cells that are several cell diameters away from a wound site are able to elongate in the direction of the wound to assist in wound closure [28]. Such observations highlight the importance of Ca^{2+} in the repair of damaged tissues and imply that Ca^{2+} may play a fundamental role in the relay of mechanical information to cells in the event of tissue damage as well as general changes in the mechanical environment. However, the scope of Ca^{2+} signaling in epithelial wound repair is still not fully understood, partly due to the largely qualitative level of analysis that has been done to date. In particular, the factors that govern the spatial extent and temporal patterning dynamics of Ca^{2+} signaling have not been elucidated.

Toward this end, we have performed a quantitative analysis of the transient intercellular Ca^{2+} flashes following localized laser ablation of cells in the pouch of the wing imaginal disc. The wing imaginal disc is a larval progenitor organ, consisting of two connected layers of epithelial cells that later develops into the adult wing and thorax (Fig. 1). The wing disc grows considerably during larval development, increasing from approximately 50 to 50,000 cells [29,30]. It consists of a simple and relatively flat epithelial cell sheet and has been intensively studied as a model for pattern formation and size control during epithelial organogenesis [18,31]. The larval wing disc also demonstrates extraordinary regenerative capacity and is able to fully repair and produce a correctly patterned adult wing after losing up to 50% of its cells [32], making it an important model system for studying regeneration. The wing disc also lends itself to ex vivo culture and live-imaging over the course of multiple hours [33] or more infrequently with in vivo imaging [34]. In particular, the oval-shaped wing disc pouch, which is responsible for forming the adult wing blade, is located in the center of the wing disc and is ideal for examination of Ca^{2+} dynamics in epithelia due to its relative flatness and optical accessibility.

The pouch is divided into well-defined developmental compartments separated by anterior-posterior (AP) and dorsal-ventral (DV) axes (Fig. 1A, B).

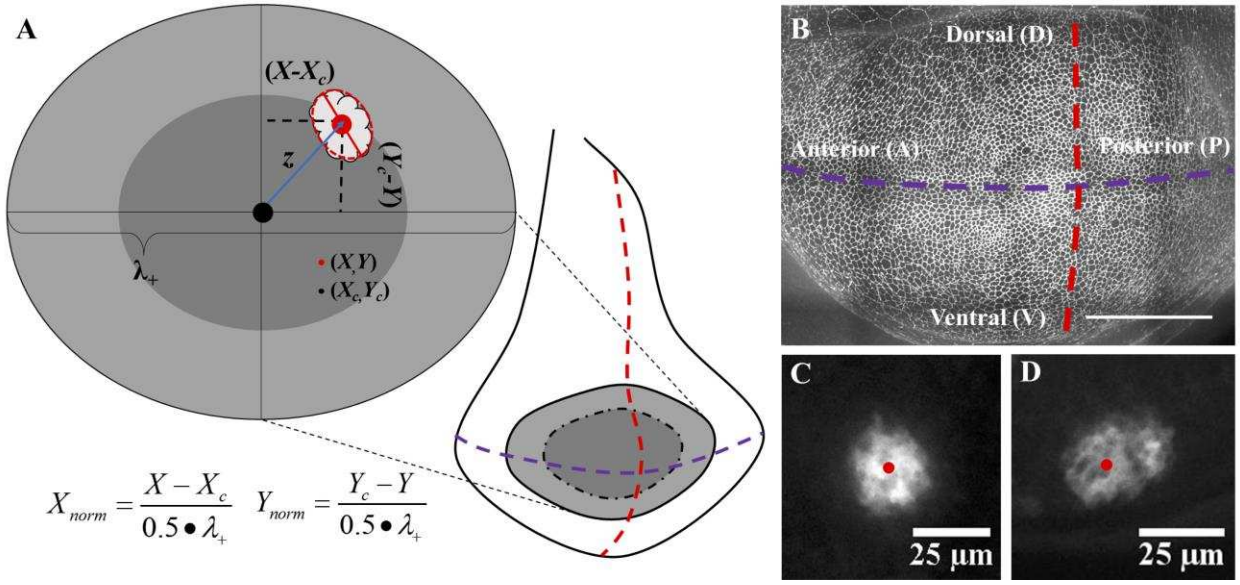

FIGURE 1. The Drosophila wing imaginal disc represents a versatile system for the study of wound-induced Ca^{2+} flashes. The wing disc is a relatively simple tissue, which exhibits extraordinary wound healing capacity. (**A**) Schematic of a full wing disc with the pouch shown in grey. The major developmental axes, the anterior-posterior (AP) (red) and dorsal-ventral (DV) (purple) are also shown. Flashes were classed based on the normalized distance between the flash centroid and the pouch centroid, z, as being either central ($0.50 \geq z$) or peripheral ($0.50 < z$). (**B**) Confocal image of a typical 3rd instar wing disc pouch. Here, cell boundaries are visualized with fluorescently-tagged E-Cadherin, DECad::GFP. The scale bar is 50µm. (**C**) Characteristic Ca^{2+} flash occurring near the pouch center (z=0.2). (**D**) Characteristic flash situated near to the pouch periphery (z=0.9). In **C** and **D**, red dots mark the ablation target.

Similar to Ca^{2+} flashes in the embryo and pupal notum, we find that localized ablation in a Drosophila wing disc pouch induces a Ca^{2+} flash that propagates across multiple cell diameters [24,26]. Observations of Ca^{2+} flash dynamics from multiple discs reveal conserved qualitative features of the flash, in particular, the formation of spatially asymmetric elliptical profiles farther from the center of the pouch (Fig. 1C, D). To explain this spatial variation in asymmetry, we analyzed computational simulations of intercellular Ca^{2+} dynamics. From an examination of the previous literature and an initial pharmacological study in the wing disc, we chose a model based on the regulation of Ca^{2+} transport into the cytoplasm from endoplasmic reticulum (ER) stores, which is stimulated by the kinetics of IP_3. Stimulation by IP_3 is a conserved mechanism through which Ca^{2+} signals are transduced in many model tissues and has been used successfully in the past to recapitulate both qualitative and quantitative features of mechanically-induced Ca^{2+} flashes in computational models [8,35–37]. Here, we have quantified the dynamics of Ca^{2+} flashes in developing Drosophila wing discs, which exhibit both cell size and anisotropy gradients across the epithelium. Comparison between experimental and computational results supports the determination that the spatial asymmetry in Ca^{2+} propagation is principally

explained by a gradient of cell shape anisotropy present across the proximal-distal axis of the disc. Although not a significant input to flash anisotropy, the gradient of apical cell area **impacts** the total flash area and velocity of the flash.

2. MATERIALS AND METHODS

2.1 Fly lines and genetics

The GCaMP6f Ca^{2+} sensor [20] was expressed ubiquitously in 3rd instar wing imaginal discs or constrained to the wing disc pouch using the GAL4-UAS system - tub-GAL4>UAS-GCaMP6f and nub-GAL4>UAS-GCaMP6f, respectively[38]. To visualize cell boundaries for the purpose of examining cell size distribution within the wing disc, discs from 3rd instar larvae of DE-Cadherin::GFP were used [39]. All flies were raised at 25 ^{o}C and 70% relative humidity on standard culture medium, and crosses were made using standard techniques [40].

2.2 Laser ablation experiments and Ca^{2+} visualization

Third instar wing imaginal discs from tub-GAL4>UAS-GCaMP6f larva were dissected and cultured in an ex vivo disc imaging chamber described previously [33]. Discs were cultured in Schneider's Drosophila media with 6.2 μg/mL insulin (Sigma Aldrich, Saint Louis, MO) and 0.5% (v/v) penicillin-streptomycin (Gibco (10,000 U/mL), Grand Island, NY). Imaging was performed on a Nikon Eclipse Ti confocal microscope (Nikon Instruments Inc., Melville, NY) with a Yokogawa spinning disc and MicroPoint laser ablation system (Andor Technology, South Windsor, CT). Image data were collected on an iXonEM+ cooled CCD camera (Andor Technology, South Windsor, CT) using MetaMorph® v7.7.9 software (Molecular Devices, Sunnyvale, CA). All experiments were performed immediately following dissection to minimize time in culture. Discs were imaged at a single z-plane, 40x magnification and 1-second intervals for a total period of five minutes. At five seconds into the time-lapse recording, a point ablation was performed by targeting the approximate center of a single cell in the pouch for 0.2 seconds to stimulate a Ca^{2+} response. The relative size and extent of a characteristic ablation is shown in Supplementary Material, Fig. S1. Multiple spatially separated ablations (up to nine) were performed on each cultured disc in order to capture dynamics across the full extent of the pouch. Each ablation occurred at a unique location in different regions to ensure that previous ablations did not interfere with the propagation of subsequent experiments. As the extent of the 3rd instar pouch is larger than the field of view at 40x magnification, multiple tiles were stitched together in post-processing to create a picture encompassing the entire disc pouch.

2.3 Pharmacological investigation of the Ca^{2+} flash response

Third instar wing imaginal discs were dissected as above in the media described with addition of either 2-ABP (IP_3 receptor – IP_3R) [41], thapsigargin (sarco/endoplasmic reticulum Ca^{2+}-ATPase - SERCA) [42], carbenoxolone (gap junctions) [43], dantrolene (ryanodine receptor - RyR) [44], ruthenium red (RyR) [45], or LY294002 (phosphoinositide 3-kinase - PI3K) [46]. Each of these was selected to inhibit the particular component of the Ca^{2+} pathway (in parenthesis). Discs were incubated in media with or without the selected compound for one hour before ablation and imaging (as above). Thapsigargin and dantrolene were obtained from Enzo Life Sciences (Farmingdale, NY); 2-APB, ruthenium red, and LY294002 were obtained from Tocris Bioscience (Bristol, UK); carbenoxolone was obtained from Sigma Aldrich (St. Louis, MO).

2.**4** Image processing and analysis

Time-lapse videos of Ca^{2+} flashes were analyzed with the open-source software Fiji [47]. A projection of average pixel intensity with time was performed on each of these video stacks to provide an accurate picture of each flash centroid with landmark features from the pouch background and the resulting tiles manually stitched using the plugin MosaicJ [48]. The flashes in each stitched pouch were manually segmented by thresholding the stitched pouches using the 'Default' setting and added to the Region of Interest (ROI) manager using the 'Analyze Particles…' function. The entire pouch was manually outlined by an arbitrary n-sided polygon and the centroid of this polygon calculated to provide the pixel coordinates of the pouch center. An ellipse was also fit to this defined polygon to define the major and minor axes for the purposes of normalization. A custom Fiji macro was then applied to each flash ROI to provide relevant distance and slope measurements from the pouch centroid to the flash centroid.

To compensate for size variation between pouches, the absolute distance in x and y from the pouch centroid to the flash centroid was normalized by dividing by the length of the major axis of the best-fit ellipse for the pouch (Fig. 1A). For a quantitative description of flash asymmetry, the standard deviation projection for each flash was generated to provide a clear spatial outline of the flash with minimal background. These flashes were segmented using the Yen autothresholding algorithm [49], which provided a robust and accurate segmentation in all cases observed. The segmented individual flashes were added to the ROI manager in Fiji and a second custom macro was run to calculate the fractional anisotropy of the flash, S. This quantity is defined in terms of the major and minor axes of the best-fit ellipse for each flash, denoted by λ_+ and λ_-, respectively, as follows [34],

$$S = \frac{|\lambda_+| - |\lambda_-|}{|\lambda_+| + |\lambda_-|} \qquad (1)$$

Flashes were classed based on the normalized distance between the flash centroid and the pouch centroid, z, as being either central ($0.50 \geq z$) or peripheral ($0.50 < z$). MATLAB was used to generate a series of boxplots comparing the morphological and kinetic features of the flashes from each class. The analysis encompassed a total of 40 flashes from a sample of nine 3rd-instar wing discs. The Fiji macros and MATLAB code used in the above analysis are provided in the Supp**lementary** Material.

2.**5** Determination of cell size distribution

Third instar DE-Cadherin::GFP wing discs were fixed in 4% formaldehyde solution and imaged on the microscope system described above at 100X magnification with a z-stack interval of 0.5 µm. The entire pouch was imaged using a 6x6 grid of individual image tiles with 10% overlap at the boundaries. Individual grid tiles were stitched into a high-resolution, whole-pouch montage using Fiji [47]. Cell shapes in the wing disc pouch were segmented using Seedwater Segmenter [50]. A sample of 12,349 cells from three 3rd instar wing discs was used. ImageJ was used to define an ellipse fitting the segmented pouch and the ellipse cropped to remove cells in the field of view that lay outside the bounds of the pouch. Next, cells on the boundary of this ellipse that were cropped such that the entire cell was no longer visible were removed using the flood-fill tool in ImageJ. A custom MATLAB script (see Supplementary Material) was used to determine the centroid of the pouch, the individual cell centroids, the convex apical cell areas and

major/minor axes for each cell. Cell data were then sorted by convex area and the upper and lower 2% of cells cropped from further analysis to remove additional errors in the segmentation mask, which typically lie at either extreme. Color-coded maps of cell size and fractional anisotropy across the disc were generated using MATLAB.

2.6 Mathematical model for intercellular Ca^{2+} signaling

A number of mathematical models describing different aspects of intracellular Ca^{2+} dynamics have been developed previously [51]. Here we focus on a two-dimensional model describing the dynamics of intracellular Ca^{2+} previously developed for epithelial cells (Fig. 2A). A central process in this model is the release of Ca^{2+} from the ER into the cytoplasm, which is regulated by channels sensitive to the messenger molecule IP_3. An injury or mechanical stress to a cell can trigger activation of IP_3 within the cell that, in turn, binds to IP_3R on the store membranes, opening ion channels and releasing Ca^{2+} into the cytoplasm [52]. IP_3-receptors are associated with Ca^{2+}-induced- Ca^{2+}-release (CICR): a process in which the uptake of cytoplasmic Ca^{2+} by IP_3R induces a release of Ca^{2+} from the internal stores. In this way, CICR increases the cytoplasmic concentration of Ca^{2+} in the short term. There is also a continuous pumping of Ca^{2+} from the cytoplasm into the ER through the SERCA pump [53]. Cytoplasmic Ca^{2+} and IP_3 may also diffuse to neighboring cells through gap junctions, thus propagating the activation and causing a distinct flash within the tissue [24,54,55]. The presence of both IP_3 and IP_3R have already been confirmed in Drosophila in previous studies and linked to CICR and Ca^{2+} homeostasis in multiple Drosophila tissues [46,56–59]. Antibody stains for IP_3R have also previously demonstrated the presence of IP_3R in the wing imaginal disc [60]. In the present study we link IP_3 to a Ca^{2+} flash response in the wing disc using a pharmacological screen of major Ca^{2+} pathway components (see Supplementary Material, Table S1).

To provide a simple model description that can account for the Ca^{2+} flash geometry, a continuum description with no explicit definition of individual cells was used to model intercellular Ca^{2+} dynamics within the wing disc pouch. This avoids the introduction of interior boundary conditions at individual cell membranes within the spatial domain and greatly increases the computational tractability and domain size that can be simulated. Without an explicit definition of cells, quantities representing the magnitude of cell size and cell anisotropy can be imposed on the tissue domain and easily varied to rapidly test the effects of model parameters on patterning of the Ca^{2+} flash.

The model is dependent on a single intracellular pool of Ca^{2+} and IP_3. It consists of the following system of coupled ordinary and partial differential equations that describe how the concentrations of Ca^{2+} and IP_3 vary in time and space [35]. Approximating a region of the wing disc pouch by a two-dimensional square domain of length L in x and y, we have

$$\frac{\partial P}{\partial t} = D_P^{intra}\left(\frac{\partial^2 P}{\partial x^2} + \frac{\partial^2 P}{\partial y^2}\right) - \frac{V_P P k_P}{k_P + P} \quad (2)$$

$$\frac{\partial C}{\partial t} = D_C^{intra}\left(\frac{\partial^2 C}{\partial x^2} + \frac{\partial^2 C}{\partial y^2}\right) + J_{flux} - J_{pump} + J_{leak} \quad (3)$$

$$\frac{dh}{dt} = \frac{1}{\tau_h}\left(\frac{k_2^2}{k_2^2 + c^2} - h\right) \quad (4)$$

Here P(x, y, t), C(x, y, t) and h(t) denote the concentration of IP_3, the concentration of Ca^{2+} and the fraction of IP_3 receptors that have not been inactivated by Ca^{2+} at time $t \geq 0$ and position $(x, y) \in [0, L] \times [0, L]$, respectively. The Ca^{2+} fluxes J_{flux}, J_{pump} and J_{leak} represent the processes described above and schematized in Fig. 2. We use the functional form of the Ca^{2+} fluxes proposed previously [35], namely

$$J_{flux} = k_{flux}\mu(P)h\left[b + \frac{(1-b)C}{k_1 + C}\right] \quad (5)$$

$$J_{pump} = \frac{\gamma C^2}{k_\gamma^2 + C^2} \quad (6)$$

$$J_{leak} = \beta \quad (7)$$

The function $\mu(P)$ models the activation of the IP_3 receptor by IP_3 and is chosen to take the form

$$\mu(P) = \frac{P}{k_\mu + P} \quad (8)$$

The form of μ(P) was chosen from a previously developed model [35] to match experimental observations that the flash intensity is highest at the point of stimulation and decreases with radial distance. All model parameters along with their interpretations and values are given in Table 1. We note that the effective intracellular diffusion coefficient of IP_3 given in Table 1 is far greater than that of Ca^{2+}, implying that IP_3 will diffuse through the cell much faster than Ca^{2+}. Although Ca^{2+} ions are much smaller than IP_3 molecules, the presence of Ca^{2+} buffers in the cytoplasm significantly slow down the intracellular diffusion of Ca^{2+}, while the cell's internal structures slow diffusion of both Ca^{2+} and IP_3 [61].

Parameter	Symbol	Value
Ca^{2+} flux when all IP_3 receptors are open and activated	k_{flux}	8 μM s^{-1}
Fraction of activated IP_3 receptors at zero Ca^{2+}	b	0.11
K_m for activation of IP_3 receptors by Ca^{2+}	k_1	0.7 μM
K_m for inactivation of IP_3 receptors by Ca^{2+}	k_2	0.7 μM
Time constant for inactivation of IP_3 receptors by Ca^{2+}	τ_h	0.2 s^{-1}
K_m of ER Ca^{2+} pumps	k_γ	0.27 μM
Maximum pump rate for the ER pumps	γ	1.1 μM s^{-1}
Rate of Ca^{2+} leak from the ER	β	0.15 μM s^{-1}
K_m for binding of IP_3 to its receptor	k_μ	0.01 μM
Maximal IP_3 degradation rate	V_P	0.08 s^{-1}
[IP_3] at which IP_3 degradation rate is half maximal	k_P	0.5 μM
Ca^{2+} diffusion coefficient	D_C^{intra}	20 μm^2 s^{-1}
IP_3 diffusion coefficient	D_P^{intra}	300 μm^2 s^{-1}
Intercellular permeability to IP_3	α_P	0.2 μm s^{-1}
Intercellular permeability to Ca	α_C	0.05 α_P
Length scale of individual cell (cell size)	l	2-6 μm
Fractional anisotropy of cell (cell elongation)	S	0 - 0.7
Length of tissue domain	L	80 μm

TABLE 1 Parameter values used in the computational model. Baseline values are taken from [35]. The values of k_{flux}, **γ, k_P** and the intercellular permeabilities were tuned to match the spatial extent and characteristic timescale of the experimentally observed flashes.

Equations (2) - (8) were originally derived for the intracellular dynamics of Ca^{2+} and IP_3 [35,36,62]. To describe their intercellular dynamics, we must incorporate the passage of these species through gap junctions into neighboring cells. Gap junctions at cell membranes severely slow down the rate at which both Ca^{2+} and IP_3 propagate throughout a tissue. We represent this in the model by using approximate expressions for the effective intercellular diffusion coefficient tensors D_C and D_P as shown in (9) and (10). These approximate expressions may be derived using homogenization techniques which rely on the assumption that the ratio of a typical cell diameter to the width of the tissue is small [8]. For the third instar larvae examined here, the wing disc pouch typically consists of several thousand individual cells on the order of 2-6 μm in diameter while the pouch itself is >100 μm in diameter. To investigate the error introduced by this assumption, we examined a 1D cell-based model and compared the simulation output to the continuum case and find that the introduced error is less than one cell diameter at maximal flash propagation. For our flashes, which propagate across approximately 10 cell diameters this error is <10% (see Supplementary Material, Fig. S2). For elongated cells (for which the fractional anisotropy, S, is non-zero), these approximate expressions are anisotropic as described below.

To obtain an approximate expression for each intercellular diffusion coefficient tensor, we assume that cells within our region of tissue may be approximated by rectangles aligned with the x and y axes, of length l and width jl. Without loss of generality we specify the aspect ratio, j, to take values in [0, 1]. We arrive at a closed-form expression for the effective intercellular diffusion coefficient tensor for Ca^{2+}, D_C, which is given by

$$D_C = \begin{pmatrix} D_C^x & 0 \\ 0 & D_C^y \end{pmatrix} = \begin{pmatrix} \left(1/D_C^{intra} + 1/l\alpha_C\right)^{-1} & 0 \\ 0 & \left(1/D_C^{intra} + 1/jl\alpha_C\right)^{-1} \end{pmatrix} \quad (9)$$

$$C_{SS} = \sqrt{\frac{\beta k_\gamma^{\ 2}}{\gamma - \beta}} \quad (10)$$

where D_C^{intra} is the intracellular diffusion coefficient of Ca^{2+} and α_C is the permeability of the cell membrane to Ca^{2+}. The expression for D_P takes a similar form. For further details on the use of homogenization theory to derive effective intercellular diffusion coefficients, see for example [8].

We assume each intracellular diffusion coefficient and permeability coefficient to be constant and spatially uniform. It is reasonable to assume an isotropic intracellular diffusion coefficient as this has been shown to recapitulate experimental observations in a number of model systems [8,36]. Since experimental mRNA evidence suggests that gap junctions are spatially uniform in the developing wing disc, it is assumed that the properties of the cell membrane can be approximated as homogenous [47]. Thus, we assume constant spatial permeability of cell membrane to both IP_3 and Ca^{2+} [54]. We further assume that membrane effects are the major source of anisotropy in any direction. We assume that the cell size l and aspect ratio j vary over length scales across the wing imaginal disc that are much larger than l, and thus that we may substitute these parameters with slowly varying functions of position in equation (9) in order to study the effect of variations in these quantities on the shape of the resulting Ca^{2+} flash.

For consistency of notation, we express the aspect ratio, j, in equation (9) in terms of the fractional anisotropy, $j = (1 - S)/(1+S)$, in the following. To close the model, we supplement equations (2)–(9) with zero-flux boundary conditions at each edge of the tissue ($x = 0$, $x = L$, $y = 0$, $y = L$). The laser ablation initial condition is modeled using an integrated IP_3 stimulus of 0.01 μM from $t = 0$ s to $t = 0.2$ s for a small 4 μm diameter circular element at the center of the domain. The IP_3 stimulus induces a Ca^{2+} flash event. IP_3 has been shown to stimulate a Ca^{2+} response in multiple cell types [26,37]. Further, it has been demonstrated previously that IP_3 will diffuse much faster than Ca^{2+} in a tissue within a range of physiological concentrations due to the presence of Ca^{2+} buffers in the cytoplasm [61]. This indicates that the observed Ca^{2+} flash is essentially a diffusive wave of IP_3 triggering Ca^{2+} release in adjoining cells rather than diffusion of Ca^{2+} from the initially stimulated cell. In the rest of the domain we impose a spatially uniform initial condition at $t = 0$, with P and h taking the values zero and one respectively. C takes its steady-state value according to equation (10).

We solve the model numerically using a simple explicit finite difference method with spatial step size $\Delta x = \Delta y = 0.5$ μm and time step $\Delta t = 0.001$ s, chosen small enough to ensure numerical

stability. A MATLAB implementation of this numerical scheme is provided in the Supplementary Material.

3. RESULTS AND DISCUSSION

3.1 Pharmacological characterization of laser induced Ca^{2+} flashes.

To test the role of gap junctions in propagating the flash response, we incubated discs for 1 hour in 30 μM carbenoxolone, a widely used gap junction inhibiter [43]. Incubation of the disc with carbenoxolone (Cbx) resulted in dramatically reduced flash propagation when compared to controls (Fig. 2 B,C). This suggests that propagation of Ca^{2+} and IP_3 through gap junctions into neighboring cells is required for propagation of the induced flash. In order to determine the role of IP_3 mediated intracellular Ca^{2+} release in flash propagation, a series of compounds targeting IP_3R, PI3K and SERCA were tested. IP_3R interacts with IP_3 in order to initiate a release of Ca^{2+} from the intracellular stores in the ER [63]. IP_3R was targeted by incubation of the wing disc for 1 hour with 200-400 μM 2-aminoethoxydiphenylborane (2-APB), a widely used inhibitor of IP_3-mediated Ca^{2+} release [41]. PI3K is involved in the production of IP3 and was targeted by incubation for 1 hour with 300 μM LY294002 (LY), a known inhibitor of PI3K that has been demonstrated to dampen wave propagation during Drosophila oocyte activation [46]. We see a dramatic reduction in flash propagation when discs are incubated with LY294002 (Fig. 2 B,D) or 2-ABP (Fig. 2 B,E). Taken together, these results strongly suggest an active role for IP_3 mediated Ca^{2+} release in the formation and propagation of the flash response. SERCA is the primary path by which cytosolic Ca^{2+} is pumped back into the ER to maintain a proper cytosolic Ca^{2+} concentration. SERCA was targeted by incubation for 1 hour with 50 μM thapsigargin (Thap), a widely used, non-competitive inhibitor of SERCA [42,64]. After incubation with thapsigargin discs demonstrated highly elevated levels of cytosolic Ca^{+2} (Fig. 2 B, F) [65,66]. Thapsigargin did not have any noticeable impact on the extent of the Ca^{2+} transient. Although noticeably dimmer, this is likely an artifact of the highly elevated background levels of GCaMP signal. Surprisingly, this is contrary to flashes induced in the embryonic epidermis, which show marked flash reduction when treated with 1 μM thapsigargin [26]. However, these observations are consistent with results from our computational model, which show a marked increase in cytosolic Ca^{2+} for increases in k_γ (increasing K_m of the SERCA pump) and reductions in γ (maximum pumping rate for the SERCA pump). These parameters also show negligible effect on maximum flash area and are not expected to significantly alter flash the propagation (see Supplementary Material). In fact, the steady state concentration of Ca^{2+} for the model simulations is entirely dependent on these two parameters and β (constant cytoplasmic leak from the ER) and takes the form of equation (10).

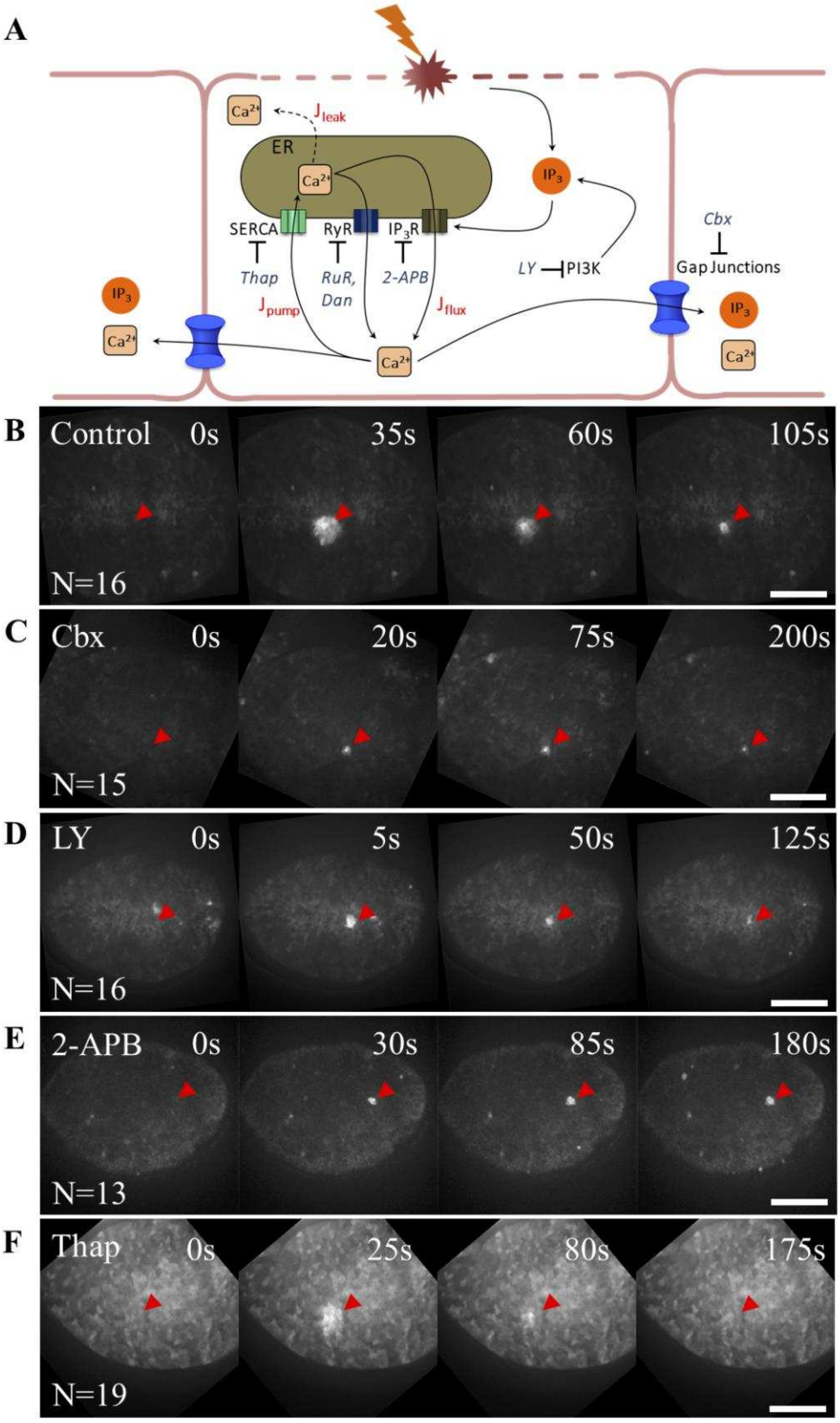
A
Ca2+
J leak
ER
Ca2+
IP3
SERCA
RyR
IP3R
Thap
RuR, Dan
2-APB
J pump
J flux
LY
PI3K
Cbx
Gap Junctions
IP3
Ca2+
IP3
Ca2+
B
Control
0s
35s
60s
105s
N=16
C
Cbx
0s
20s
75s
200s
N=15
D
LY
0s
5s
50s
125s
N=16
E
2-APB
0s
30s
85s
180s
N=13
F
Thap
0s
25s
80s
175s
N=19

FIGURE 2 . (A) Schematic of the model of intracellular Ca^{2+} dynamics in response to wounding, driven by the triggering of inositol 1,4,5-trisphosphate (IP_3) dependent release of internal Ca^{2+} stores from the endoplasmic reticulum (ER) through activation of the IP_3 receptor (IP_3R). Cytoplasmic IP_3 then diffuses to neighboring cells through gap junctions, inducing a similar response, thus propagating a Ca^{2+} flash across several cells at the wounding site. Ca^{2+} in the cytoplasm is also continuously pumped back into the ER by the sarco/endoplasmic reticulum Ca^{2+}-ATPase (SERCA) pump. A slow leak of Ca^{2+} through the ER membrane (J_{leak}) also adds to cytosolic Ca^{2+}. Figure adapted from [35]. Pharmacological targeting of relevant Ca^{2+} pathway components shown by negative inhibition arrows. Thapsigargin (Thap) inhibits SERCA, ruthenium red (RuR) and dantrolene (Dan) inhibit RyR, 2-APB inhibits IP_3R, LY294002 (LY) inhibits PI3K (IP3 production) and carbenoxolone (Cbx) inhibits gap junctions. (B) Representative Ca2+ flash under normal culture conditions. (C) Ablation in tissue incubated for one hour with 30 μM carbenoxolone shows severely limited propagation of the Ca2+ transients. (D) Ablation in tissue incubated for one hour with 200 μM LY294002 shows severely limited propagation of the Ca^{2+} transients when IP3 production is inhibited. (E) Ablation in tissue incubated for one hour with 400 μM 2-APB shows severely limited propagation of the Ca2+ transients. (F) Ablation in tissue incubated for one hour with 50 μM thapsigargin shows elevated levels of cytosolic Ca^{2+} consistent with deactivation of the SERCA pump and reduced flash propagation. All scale bars are 50 μm.

In order to ensure that flash propagation was not due to the actions of ryanodine, another small molecule responsible for Ca^{2+} release from intracellular stores, we incubated discs with two separate inhibitors of the ryanodine receptor (RyR) – dantrolene (Dan) and ruthenium red (RuR) [44,45]. Neither inhibitor had any noticeable impact on the extent of flash propagation (Supplementary Material, Fig. S3).

3.2 Spatiotemporal dynamics of wound-induced intercellular Ca^{2+} flashes

Laser ablation in the wing imaginal disc pouch creates a Ca^{2+} flash that propagates to adjacent cells followed by a recession from the maximal extent of the flash back toward the ablated cell (Fig. 3A and Fig. S1). This observation is similar to recent experiments performed in the Drosophila embryonic epidermis and pupal notum which note similar flash events [24,26]. Cells in the embryonic epidermis tend to elongate preferentially with mechanical forces during embryogenesis and it was observed that the induced flashes tended to elongate preferentially in the direction of cell elongation [26,28]. This is consistent with our results. Similar to our results with carbenoxolone, Innexin-2 null alleles caused a dramatic reduction of flash propagation. However, it was noted in the embryonic epidermis that treatment with 1 μM thapsigargin drastically reduced the extent of the flash. We did not observe a reduction in flash response in the wing imaginal disc when treated with 50 μM thapsigargin and observed elevated levels of cytosolic calcium.

Several key features are well conserved across an experimental set of 40 flashes in nine imaginal discs. Notably, ablations performed near the pouch periphery form more asymmetric shapes (Fig. 3B), which are generally elliptical ($S_{mean} = 0.15 \pm 0.06$, $S_{max} = 0.30$), than ablations performed near the pouch center ($S_{mean} = 0.09 \pm 0.05$, $S_{max} = 0.21$), which tend to be more circular ($p = 0.002$, single-factor ANOVA). This tendency towards elongation was quantified using the fractional anisotropy of the flashes. Flashes were scored as being either 'central' (N = 16) or 'peripheral' (N = 24) based on their normalized distance from the pouch centroid, z.

Flashes were further characterized by detailed analysis of their temporal area profile (Fig. 3A). Each flash was plotted and characterized by three basic parameters: full width at half max area (time scale), slope at first half max area (areal expansion rate), and slope at last half max (areal recession rate). We notice a distinct shift in the rate of change of flash area during flash recession. This shift takes the form of a dramatic reduction in the slope of the area curve (Fig. 3A) that is well conserved in 36/40 flashes. Previous work has suggested that gap junctions are gated channels which close as a function of increasing Ca^{2+} concentration and pH to protect surrounding tissue from the toxic effects of these ions [67,68]. In general, our observed shift in dynamics occurs during the recession of the flash after maximum area has been achieved. Maximum area is also achieved early in the temporal profile due to rapid initial propagation. It is likely that this shift in dynamics is due to the results of this gating effect slowing the flow of Ca^{2+} through the gap junctions in the cell membrane as cytosolic Ca^{2+} concentration rises rapidly after perturbation. Although we observe a significant difference ($d = 1.3$, $p < 0.01$) between the areal propagation rate ($r = 30 \pm 20\ \mu m^2/s$) and the areal recession rate ($r = 10 \pm 10\ \mu m^2/s$) across the entire set of 40 flashes, we see no significant difference between these rates with respect to center versus peripheral flashes (Fig. 3E, F). We also do not see any significant patterning of flash timescale across the tissue (Fig. 3D). Cohen's d is used as a metric of effect size for large data sets where significance testing by p-values becomes misleading [69]. Both the effect size and p-value, where appropriate, are reported for direct comparison.

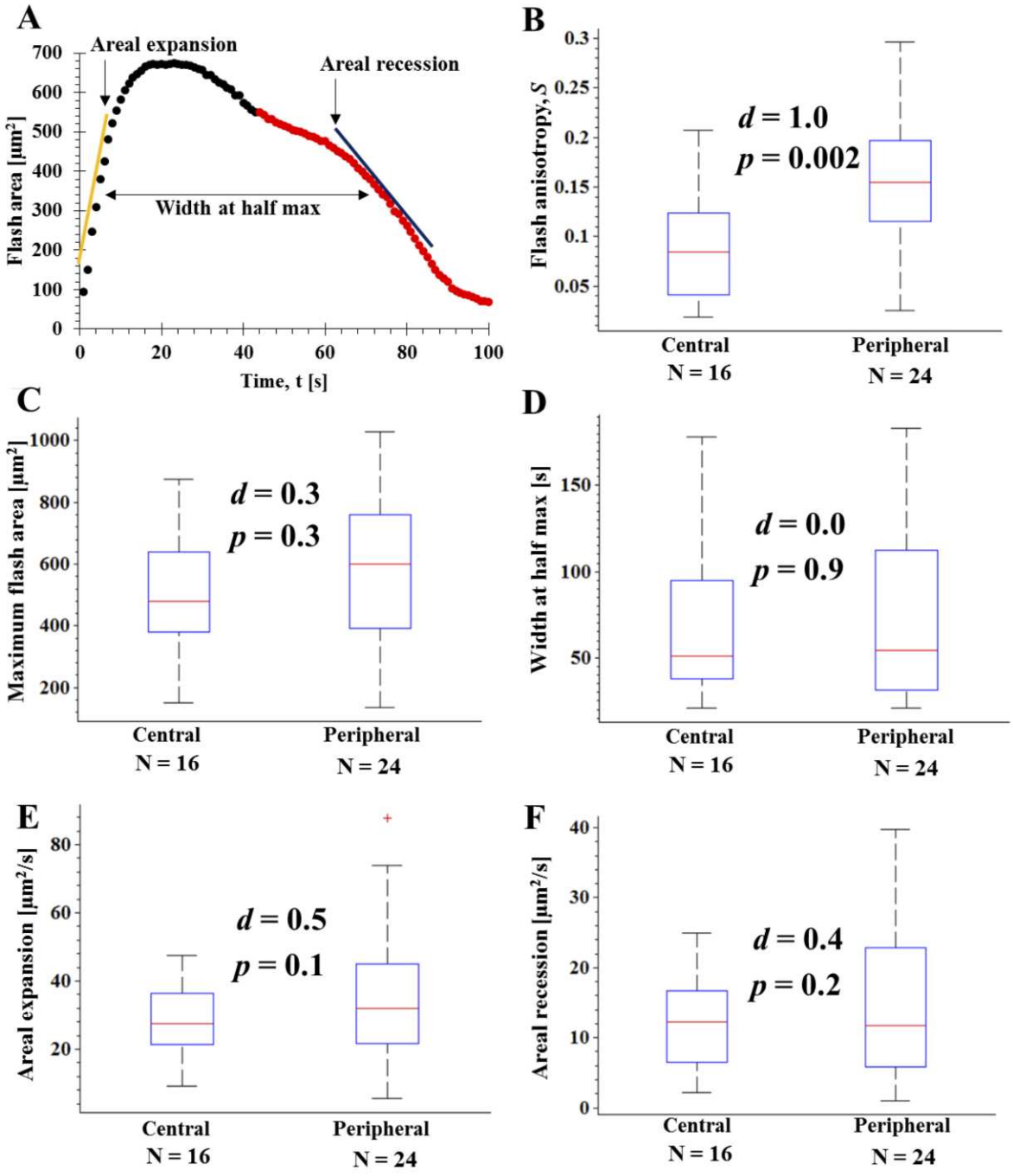

FIGURE 3. (**A**) Characteristic plot of experimental flash area with time showing rapid initial parabolic propagation. The timescale for each flash is characterized by the full width at half maximum area. The propagation and recession of the flash is characterized by the slope of this curve at each half max point. We observe a distinct shift in the rate of change of flash area (red) during recession that is conserved in 36/40 flashes. (**B-F**) Quantification of intercellular Ca^{2+} flashes. Red lines represent median values of each category. The upper and lower ends of each box represent the quartiles at 25% and 75% probability respectively. Dashed lines indicate range of the data. Outliers are plotted as red crosses. Sample size for each category is listed below the bin. (**B**) Boxplot of flash anisotropy for laser induced flashes classed as

being either central (0.5 < z) or peripheral (0.5 ⩾ z). Cohen's d = 1.0, indicating a large effective difference between the means. p = 0.002. (**C**) Boxplot of flash maximum area. Cohen's d = 0.3, indicating a small effective difference between the means. p = 0.3 (**D**) Boxplot of flash width at half max area. Cohen's d = 0.0, indicating negligible effective difference between the means. p = 0.9. (**E**) Boxplot of flash areal expansion rate. Cohen's d = 0.5, indicating a moderate effective difference between the means. p = 0.1. (**F**) Boxplot of flash areal recession rate. Cohen's d = 0.4, indicating a small effective difference between the means. p = 0.2. All p-values from single factor ANOVA.

3.2 Comparison of cell size and anisotropy variation in 3rd instar discs

As cell size has been recently shown to be non-constant within the wing imaginal disc [34,70], the observed flash asymmetries prompted us to look more carefully at the spatial variation of cell size and anisotropy within the pouch (Fig. 4). A sample of 12,349 cells from three, 3rd instar disc pouches were segmented and cell size information was extracted using a custom MATLAB script. This revealed, as expected, that there is a tendency for cells to be smaller at the center of the pouch and that apical cell area can vary by up to a factor of three across the pouch (Fig. 4A, C). Further, a plot of cell anisotropy (Fig. 4B, D) demonstrates a tendency for cells along the pouch boundary to be more elongated than center cells. As the sample sizes are so large, p-values show highly significant results between the two regions of the disc. A more rigorous indication of size effects with Cohen's d provides an indication of how strong the effects are for the two groups irrespective of sample size [69].

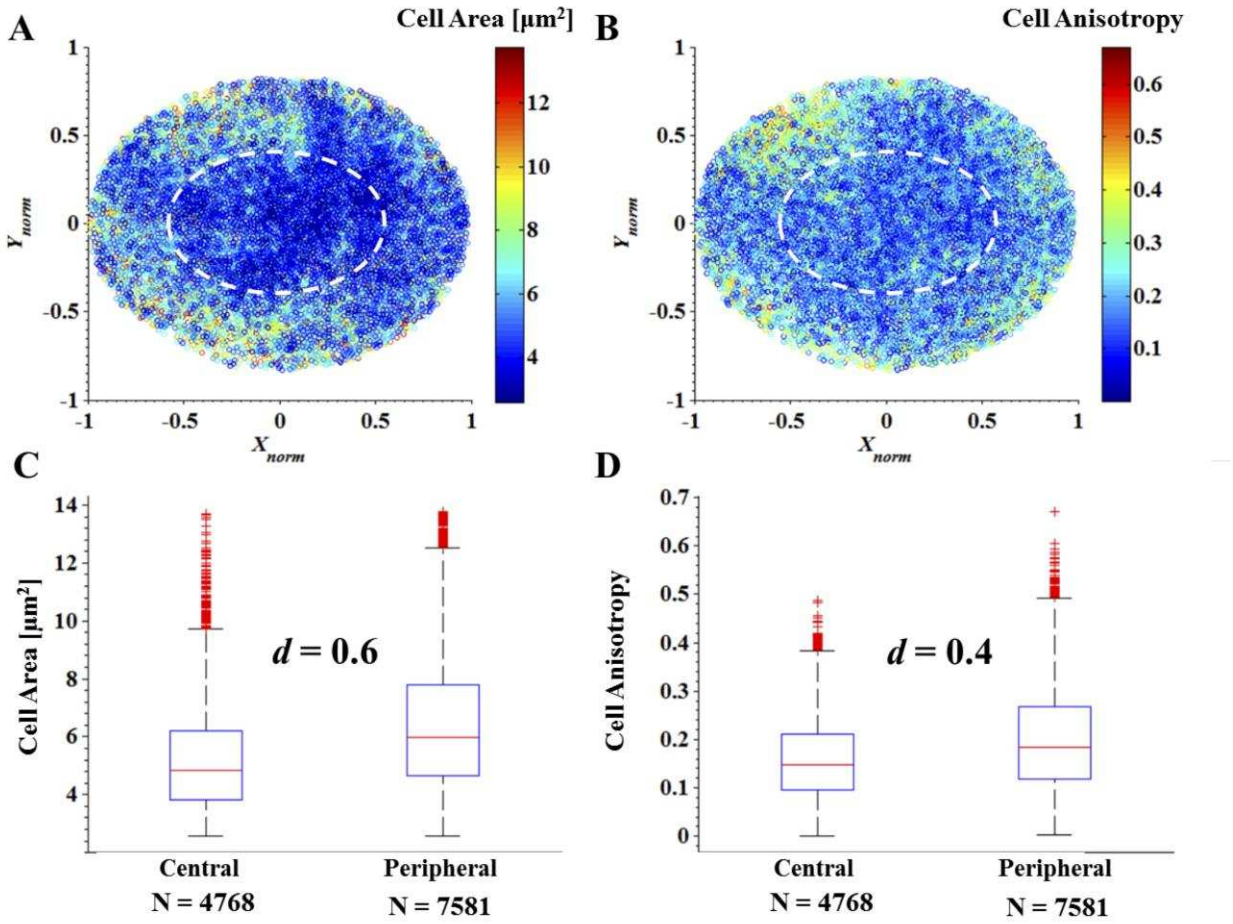

FIGURE 4. (**A**) Color-coded point cloud of 12,349 cell areas from three, 3rd instar wing imaginal discs. Note the observable qualitative increase in cell area with increasing distance from pouch center along the radial PD axis. (**B**) Color-coded point cloud of cell fractional anisotropies from the same population of cells as in (**A**). Note the observable qualitative increase in cell anisotropy with increasing distance from pouch center. White ellipses in (**A**) and (**B**) show location of z = 0.5. (**C, D**) Boxplot analysis of cell morphology. Red lines represent median values of each category. The upper and lower ends of each box represent the quartiles at 25% and 75% probability respectively. Dashed lines indicate range of the data. Outliers are plotted as red crosses. Sample size for each category is listed below the bin. (**C**) Boxplot of cell area for cells classed as being either central ($0.5 < d$) or peripheral ($0.5 \geqslant d$). Cohen's d = 0.6, indicating a medium effective difference between the means. (**D**) Boxplot of cell anisotropy. Cohen's d = 0.4, indicating a small effective difference between the means.

Experimental characterization of Ca^{2+} flash asymmetries suggests that spatial variations in these values are correlated with the observed spatial variations of both cell size and cell anisotropy in the pouch. Our analysis shows that flashes tend to develop asymmetrically in the periphery of the pouch in regions where cell size and anisotropy tend to be more variable and transition more abruptly (Fig. 4). A previous study has shown that internal mechanical forces generated during growth by proliferating cells in the wing imaginal disc play a key role in patterning cell sizes and shapes in the disc [70,71].

3.3 Computational analysis of cell geometry parameters on Ca^{2+} flash shape

As both cell size and cell shape anisotropy both vary across the PD axis, it is not immediately clear which parameter most significantly influences the observed spatiotemporal dynamics of the Ca^{2+} flashes. We used a computational model to investigate the impact of both cell size and anisotropy on the spatial spread of the flash, which allows us to vary each variable independently (Methods). This model reproduced the effect of ablating a single cell by an initial sustained increase in IP_3 in the ablated cell. IP_3 has been shown to stimulate a Ca^{2+} response in multiple cell types experimentally and computational models of IP_3 stimulated Ca^{2+} flashes have been shown to faithfully recapitulate experimentally observed Ca^{2+} data in other studies [8,35]. Further, it has been demonstrated previously that IP_3 will diffuse an order of magnitude faster than Ca^{2+} in a tissue within a range of physiological concentrations [61]. This dramatic difference in the diffusivity of Ca^{2+} and IP_3 is due to the presence of intracellular buffers which act to slow the movement of Ca^{2+} [61]. This suggests that the observed Ca^{2+} flash is essentially a diffusive wave of IP_3 triggering Ca^{2+} release in adjoining cells rather than diffusion of Ca^{2+} from the initially stimulated cell. A sensitivity analysis was performed in order to identify the model parameters most significant in influencing each experimentally measured variable, in addition to the maximum and background Ca^{2+} levels. Results of the sensitivity analysis are shown in the Supplementary Material. Maximum area and propagation rates were found to be most sensitive to IP_3 degradation and intercellular permeability of IP_3. Only minor adjustment of parameter values were necessary to obtain an in silico flash spread and timescale consistent with our experimentally observed flashes as compared to the base model developed for airway epithelial cells [35]. The maximal IP_3 degradation rate and intercellular permeability to IP_3 were increased 70% and 10% respectively over the values reported in [35] to obtain a flash timescale and maximum area in agreement with experimental data. The Ca^{2+} flux for active IP_3 receptors (k_{flux}) was increased from 3 $\mu M\ s^{-1}$, to 8 $\mu M\ s^{-1}$ to increase the maximum Ca^{2+} concentration (intensity) of the observed flash and thereby the robustness of autothresholding for subsequent analysis. The

value of k_{flux} serves only as a concentration-scaling factor in the model and does not significantly affect other aspects of the simulated flash.

In our analysis, we considered four representative scenarios to investigate the source of the Ca^{2+} anisotropy in the periphery of the wing pouch. In case I, we modeled a tissue with uniform cell size and aspect ratio across the spatial domain by setting l = 4 μm and S = 0. The chosen cell size represents the average size within our chosen range of variation for subsequent cases (2 – 6 μm), which is consistent with the three-fold increase in cell size we observed experimentally across 3rd instar wing disc pouches. In case II, the cell size, l, is varied linearly across the disc in the x-direction from 2 μm to 6 μm, $l(x,y) = 2 + 4x/L$ for $(x,y) \in [0,L] \times [0,L]$, but we preserve cell isotropy (S = 0). This case, in which the resulting effective intercellular diffusion tensors are isotropic, examines whether cell size alone explains the observed asymmetry in the Ca^{2+} flashes. In case III, the cell size is held constant across the spatial domain (l = 4 μm) but the fractional anisotropy S is varied linearly from 0 to 0.7 in the x-direction to represent cells becoming increasingly elongated along one axis of the tissue: $S(x,y) = 0.7x/L$ for $(x,y) \in [0,L] \times [0,L]$. Again, this chosen range is consistent with the experimentally observed range for the 3rd instar wing discs shown in (Fig. 4A). This case, in which the resulting effective intercellular diffusion tensors are anisotropic, examines whether cell anisotropy alone is enough to describe the observed asymmetry in Ca^{2+} flashes. In the last scenario, case IV, we vary both cell size (as prescribed for the case II) and cell anisotropy (as prescribed for case III) across the spatial domain. Simulation results for these four cases are shown in (Fig. 4).

For the chosen parameter values, we find that cell size variation across the disc produces no significant asymmetry in flash dynamics when compared to the homogeneous tissue case (Fig 5C I, II). We also observe that cells of equal size can still produce an asymmetric flash if they are sufficiently elongated (Fig. 5C I, III) and that the incorporation of heterogeneity in cell sizes does not significantly affect the asymmetry of the flash in this case (Fig 5C IV). The results of our model simulations correlate well with the experimental observations summarized in (Fig. 4) for flashes. These results demonstrate that observed variance in cell size alone is not sufficient to pattern Ca^{2+} flashes and that it is instead the extent and the direction of elongation that work to pattern the spatial extent of the Ca^{2+} flash. We also tested the extreme case of instantaneous jumps in cell size and cell anisotropy by setting each half of the domain to the respective minimum and maximum values. Even for this extreme case, we find no appreciable elongation of the computational flash for abrupt changes in cell size (Supplementary Material, Fig. S4).

3.4 Computational analysis of cell geometry parameters on Ca^{2+} flash velocity and area

The model was also used to characterize the impact of cell size and cell anisotropy on the areal dynamics and maximum area of the flash. These results are summarized in Fig. 6. For these simulations, effective size differences, ΔL, and gradient of anisotropy, ΔS, represent linear variation across the computational domain starting at minimum value of 2 μm for cell size and 0 for fractional anisotropy. For simulations with a variable cell size, the imposed anisotropy is S = 0. For simulations with variable cell anisotropy, the imposed cell size is L = 4 μm. The model suggests a linear increase in maximum flash area with increasing effective cell size and a linear decrease with increasing effective cell anisotropy (Fig. 6A, B). The model also predicts a linear increase in flash timescale and areal expansion/recession with increasing cell size (Fig. 4C, D). A corresponding linear decrease in these variables is predicted for increasing cell anisotropy (Fig.

4E, F). The predicted opposing effects of cell size and cell anisotropy on maximum area and areal propagation/recession of the flash suggest an explanation for the experimentally observed homogeneity in flash area and areal propagation/recession of the flash throughout the pouch. As

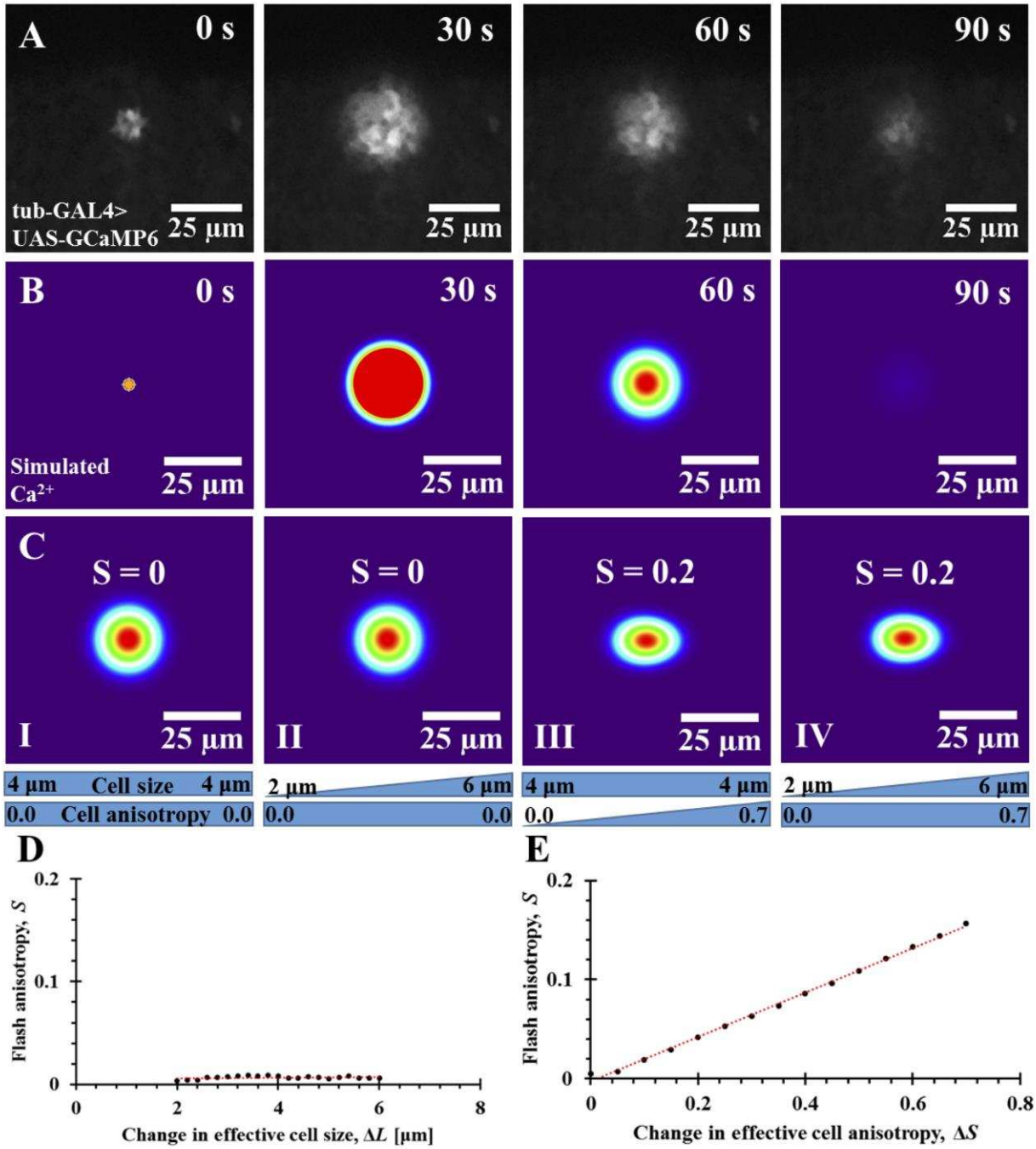

FIGURE 5. (A) Time-lapse montage of a typical experimentally observed flash from the disc periphery. **(B)** Time-lapse montage of a simulated flash involving a gradient of both cell size (2 – 6 µm) and cell anisotropy (0.0 – 0.7). **(C)** The effect of spatially varying cell size and fractional anisotropy on simulated flash dynamics. The blue bars represent the imposed variation in cell size (upper) and fractional anisotropy (lower) across the spatial domain. A non-uniform distribution of cell size, or aspect ratio, leads to a spatially non-uniform, or anisotropic, effective diffusion coefficient for each diffusible species in the

model. Frames shown are extracted at 72 s when asymmetry has reached its full extent. (**C, I)** Ca^{2+} flash with a uniform cell size (4 μm) and fractional anisotropy (S = 0). (**C, II)** Ca^{2+} flash with a gradient of cell size from 2-6 μm in the indicated direction and uniform fractional anisotropy. Propagation is still symmetric. (**C, III**) Ca^{2+} flash with uniform cell size and a gradient of fractional anisotropy from 0-0.7 in the indicated direction. Note that even with uniform cell sizes, an increase in fractional anisotropy leads to asymmetric propagation of the flash. (**C, IV**) Both a 2-6 μm cell size gradient and a 0-0.7 fractional anisotropy gradient are imposed on the sheet. There is no significant change to the asymmetry. (**D**) Graph of effective cell size gradients and their impact on flash anisotropy. Significant anisotropy does not develop for physiologically relevant gradients of cell size. Note that although cell size may vary the characteristic length in both the x- and y- directions is equal when fractional anisotropy is zero. (**E**) Graph of effective cell anisotropy gradients and their impact on flash anisotropy. Anisotropy of the flash in these cases match the experimentally observed magnitude for physiologically observed gradients in cell anisotropy.

both cell size and cell elongation effectively increase across the PD axis of the pouch, the local anisotropy works to pattern the flash asymmetrically in space, but the corresponding gradient in cell size works to balance out impact on propagation, recession and area. Previous studies have also demonstrated that the velocity of long-distance Ca^{2+} transients are remarkably constant as they travel across both epithelial and endothelial cells [72]. Our model suggests that the opposing effects of cell size and cell anisotropy offer a possible mechanism through which wave speeds are conserved in a heterogeneous, anisotropic tissue a feature that is likely a conserved in epithelial systems.

The model proposed here offers no description of Ca^{2+} concentration-dependent dynamics of gap junction permeability in the disc. Gap junctions assumed to have uniform permeability in time and space are sufficient to reproduce the experimentally observed flash elongation, maximum area, and full width at half maximum area. However, previous studies suggest that gap junctions actively close in response to high Ca^{2+} to shield neighboring cells from a toxic overdose [67,68]. Our experimental time-plots of area demonstrate a distinct shift in dynamics during flash recession that is suggestive of this drop in intercellular permeability. While the flash area increases quadratically during the initial phase of propagation, during recession, the flash follows higher-order polynomial dynamics. In contrast, the areal dynamics of our model demonstrate quadratic behavior throughout the entire simulation and we are unable to reproduce the differential propagation and recession velocities seen experimentally with our current phenomenological model. Ions other than Ca^{2+} have also been shown to reduce gap junction permeability [67,68,73]. Additionally, the exact nature of gap junction decoupling as a result of high Ca^{2+} concentration has only recently begun to be rigorously investigated [74]. Therefore, incorporation of the additional complexities introduced by Ca^{2+} dependent spatiotemporal regulation of gap junction permeability is a subject for future investigation.

4. CONCLUSIONS AND OUTLOOK

Previous studies have established the relationship between mechanical forces exerted by growth and cellular patterning in the tissue [16,75]. Recent evidence in both the wing imaginal disc and the developing embryo demonstrate that cell shape deformations correlate strongly with patterns of mechanical forces in the tissue [34,76]. These studies suggest that as the wing disc grows, cells in the center of the disc are subjected to compressive forces as the tissue expands outwards,

while cells at the edge of the tissue are subjected to tensile forces [77,78]. These forces lead to the experimentally observed gradients in cell size and cell anisotropy.

Ca^{2+} signaling is instrumental in regulating many fundamental cellular processes from proliferation to wound healing [24]. Here we investigated the fast Ca^{2+} response after wounding in 3rd instar wing discs to explore how mechanical heterogeneity in a tissue impacts Ca^{2+} signaling. We have established the role of IP_3 in propagating the observed flash response in wing discs through a pharmacological examination of the major Ca^{2+} pathway components. Inhibition of IP_3R and PI3K resulted in greatly diminished flash response. Further, chemical inhibition of gap junctions also resulted in a lack of flash propagation. We have also quantified the difference in asymmetry between flashes occurring along the pouch periphery and flashes occurring near the pouch center. Peripheral flashes tend to elongate into elliptical shapes, following the local elongation of cells around the pouch periphery. By contrast, central flashes tend to assume a more circular profile. We have demonstrated a significant difference in the asymmetry of Ca^{2+} dynamics in each of these two categories. We further showed that these observed asymmetries are consistent both with gradients of cell fractional anisotropy and cell size measured in the tissue.

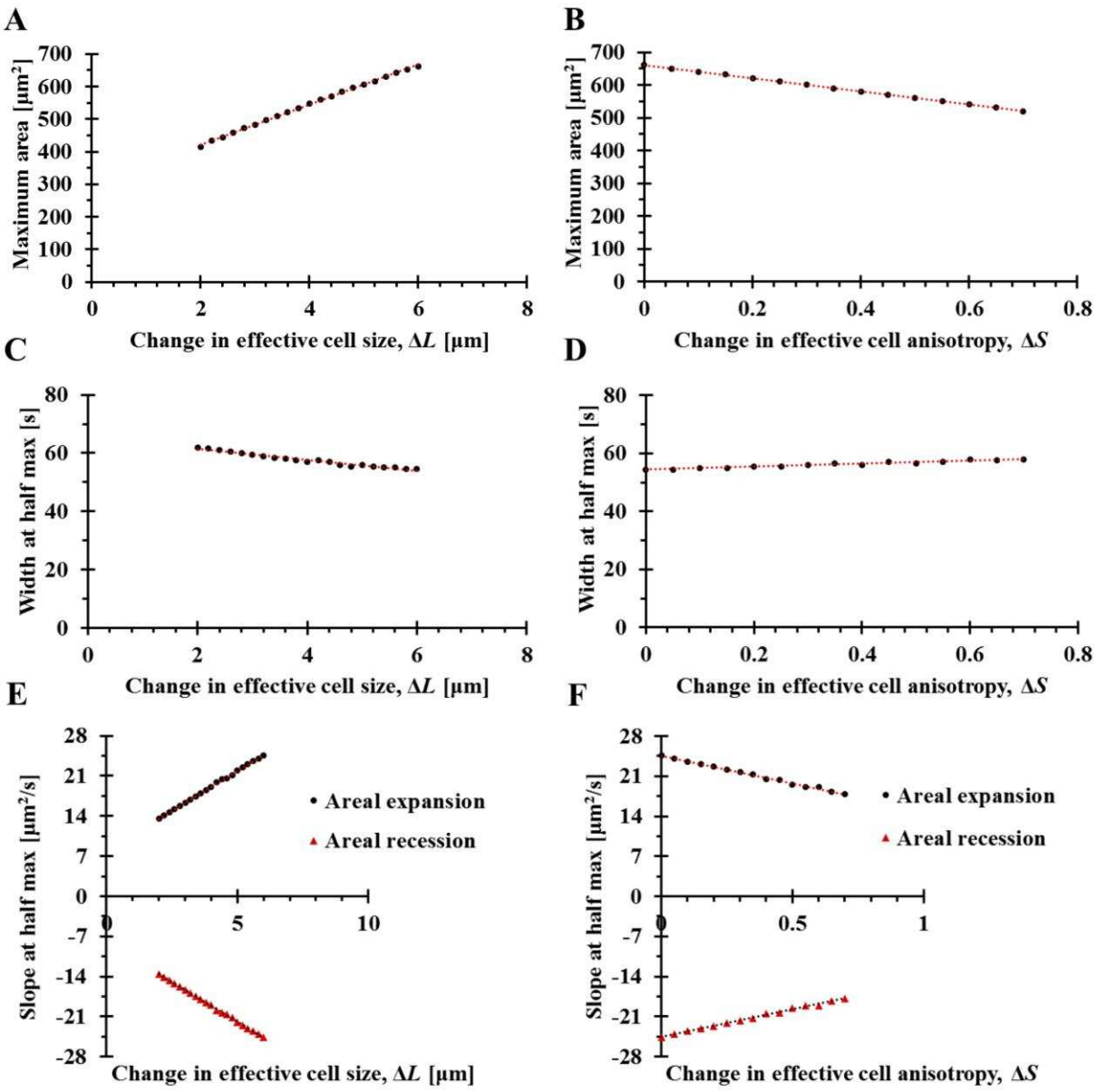

FIGURE 6. The effects of cell size and cell anisotropy on flash morphology. (**A**) Plot of maximum flash area versus effective cell size from multiple in silico simulations. Effective size differences, ΔL and ΔS, represent linear variation across the computational domain starting at minimum value of 2 μm for cell size and 0 for anisotropy. For variable cell size simulations, imposed anisotropy is S = 0. For variable anisotropy simulations, imposed cell size is L = 4 μm. (**A**) The model predicts a linear increase in flash area with increasing cell size. (**B**) The model predicts a linear decrease in flash area with increasing cell anisotropy. (**C**) The model predicts a small linear decrease in flash timescale with increasing cell size (**D**) The model predicts a small linear increase in flash timescale with increasing cell anisotropy. (**E**) The model predicts a linear increase in both areal expansion (black circles) and areal recession (**red** triangles) rate with increasing cell size. (**E**) The model predicts a linear decrease in both areal expansion (black circles) and areal recession (**red** triangles) rate with increasing cell anisotropy. All R^2 values are from linear best-fit curves. The opposing effects of cell size and cell anisotropy illustrated in (**A**)-(**F**) explain the experimentally observed homogeneity in flash velocity, maximum area and timescale.

Computational simulations allow us to decouple effects of cell size and anisotropy on intercellular Ca^{2+} signaling dynamics. To analyze the potential roles of cell size and cell anisotropy as a driving force of these observed spatiotemporal dynamics for wound-induced Ca^{2+} flashes, we compared simulation results from a computational model of Ca^{2+} dynamics to experimental data. The high level of conservation of Ca^{2+} signaling in eukaryotic systems enabled us to apply a model previously developed for epithelial tissues in other systems [35] and extend this to the epithelial cells of the Drosophila wing imaginal disc pouch. We constructed a continuum description of the intercellular Ca^{2+} dynamics by introducing effective diffusion coefficients that depend on the cell length scale and anisotropy. To enable a simple derivation of effective diffusion coefficients, we assumed cells to be rectangular: this assumption has been shown to recapitulate experimental observations in past models of mechanically stimulated **Ca^{2+}** waves in airway epithelial cells [8,35]. With this model, we found that the experimentally observed variations in flash asymmetry cannot be explained solely by a physiologically observed gradient of cell size within the tissue. We found that this asymmetry is instead most likely the direct result of heterogeneities in cell fractional anisotropy (elongation) within the tissue.

Given the established connections between cell elongation and mechanical forces within tissues, our work suggests that the observed asymmetric flashes propagate preferentially along existing lines of force within anisotropic tissues [34,70,75]. This work also demonstrates that different aspects of spatiotemporal dynamics of Ca^{2+} signaling (area, velocity, anisotropy) can be attributed to either cell size effects or cell anisotropy. We also have shown that the computational model can be used to make predictions about the spatiotemporal dynamics of the Ca^{2+} flashes within the patterned tissue, providing a guide for future studies incorporating the cellular responses to Ca^{2+} transients. Recent evidence demonstrating that Ca^{2+} signaling is correlated with waves of actomyosin recruited to the wound site in the minutes following damage suggests that these flashes may also serve to recruit subunits necessary for repair and instruct surrounding cells to elongate towards, and close, the wound [24,28]. The close coupling between cell geometry and Ca^{2+} signaling could also provide a mechanism for the transfer of information regarding cell and tissue shapes across epithelia for a given mechanical stimulus.

In related work outside the scope of this study, we observe more complicated Ca^{2+} transients in response to other stimulation modalities (manuscript in preparation). Recent studies have shown that many factors can contribute to the elongation of a cell or tissue [79] and completely decoupling these factors is a daunting challenge. It remains for future investigations whether fat and daschous mutants, which are important for P/D axis patterning, growth control, and cell polarity [80], may impact the pattern of Ca2+ flashes apart from general considerations of cellular morphometry. Microfluidic platforms might also be used to artificially alter cellular aspect ratio and observe changes to an induced Ca^{2+} response [81]. This work provides an important foundation for understanding how cell properties affect or encode information in intercellular Ca^{2+} responses. This can be expanded in the future to couple a spatiotemporal description of Ca^{2+} signaling with dynamic cell shape changes [82,83] during growth or under physical deformations to provide additional experimental evidence of the relationships uncovered in this current study.

Acknowledgements
We thank the Bloomington stock center for the tub-GAL4 (BL#5138) and UAS-GCaMP6f (BL#42747) fly lines used in this study. Additionally we would like to extend our thanks to the Notre Dame Integrated Imaging Facility (NDIIF) and other members of the Zartman lab who assisted in the experiments. We thank Jochen Kursawe, Simon Restrepo, Erin Howe and Miranda Burnette for comments on earlier versions of the manuscript. AF is funded by the Engineering and Physical Sciences Research Council through grant EP/I017909/1. CN, QW, PB and JZ were funded in part by the National Science Foundation grant CBET 1403887. PB and QW were funded partially by NIH grant UO1 HL116330. AF and JZ acknowledge funding from a Royal Society International Exchanges Scheme grant (IE130149). AF and JZ acknowledge funding from a Royal Society International Exchanges Scheme grant (IE130149). The authors thank Prof. S. Jonathan Chapman for valuable advice on the modeling.

REFERENCES

[1] Kahl C R and Means A R 2003 Regulation of Cell Cycle Progression by Calcium/Calmodulin-Dependent Pathways Endocr. Rev. **24** 719–36

[2] Orrenius S, Zhivotovsky B and Nicotera P 2003 Regulation of cell death: the calcium–apoptosis link Nat. Rev. Mol. Cell Biol. **4** 552–65

[3] Wei C, Wang X, Chen M, Ouyang K, Song L-S and Cheng H 2009 Calcium flickers steer cell migration Nature **457** 901–5

[4] Berridge M J, Lipp P and Bootman M D 2000 The versatility and universality of calcium signalling Nat. Rev. Mol. Cell Biol. **1** 11–21

[5] Markova O and Lenne P-F 2012 Calcium signaling in developing embryos: Focus on the regulation of cell shape changes and collective movements Semin. Cell Dev. Biol. **23** 298–307

[6] Dolmetsch R E, Xu K and Lewis R S 1998 Calcium oscillations increase the efficiency and specificity of gene expression Nature **392** 933–6

[7] Boyce S T and Ham R G 1983 Calcium-Regulated Differentiation of Normal Human Epidermal Keratinocytes in Chemically Defined Clonal Culture and Serum-Free Serial Culture J. Invest. Dermatol. **81** 33s – 40s

[8] Keener J P and Sneyd J 2009 Mathematical Physiology: I: Cellular Physiology (Springer)

[9] Ando J and Yamamoto K 2013 Flow detection and calcium signalling in vascular endothelial cells Cardiovasc. Res. **99** 260–8

[10] Benavides Damm T and Egli M 2014 Calcium's Role in Mechanotransduction during Muscle Development Cell. Physiol. Biochem. **33** 249–72

[11] Jones T J and Nauli S M 2012 Mechanosensory Calcium Signaling Calcium Signaling Advances in Experimental Medicine and Biology ed M S Islam (Springer Netherlands) pp 1001–15

[12] Abu Khamidakh A E, Juuti-Uusitalo K, Larsson K, Skottman H and Hyttinen J 2013 Intercellular Ca(2+) wave propagation in human retinal pigment epithelium cells induced by mechanical stimulation Exp. Eye Res. **108** 129–39

[13] Ohata H, Tanaka K, Maeyama N, Yamamoto M and Momose K 2001 Visualization of elementary mechanosensitive Ca2+-influx events, Ca2+ spots, in bovine lens epithelial cells J. Physiol. **532** 31–42

[14] Olsen S M, Stover J D and Nagatomi J 2011 Examining the Role of Mechanosensitive Ion Channels in Pressure Mechanotransduction in Rat Bladder Urothelial Cells Ann. Biomed. Eng. **39** 688–97

[15] Resnick A 2010 Use of optical tweezers to probe epithelial mechanosensation J. Biomed. Opt. **15** 015005–015005 – 8

[16] Aegerter-Wilmsen T, Smith A C, Christen A J, Aegerter C M, Hafen E and Basler K 2010 Exploring the effects of mechanical feedback on epithelial topology Development **137** 499–506

[17] Baena-Lopez L A, Nojima H and Vincent J-P 2012 Integration of morphogen signalling within the growth regulatory network Curr. Opin. Cell Biol. **24** 166–72

[18] Buchmann A, Alber M and Zartman J J 2014 Sizing it up: The mechanical feedback hypothesis of organ growth regulation Semin. Cell Dev. Biol. **35C** 73–81

[19] Shraiman B I 2005 Mechanical feedback as a possible regulator of tissue growth Proc. Natl. Acad. Sci. U. S. A. **102** 3318–23

[20] Chen T-W, Wardill T J, Sun Y, Pulver S R, Renninger S L, Baohan A, Schreiter E R, Kerr R A, Orger M B, Jayaraman V, Looger L L, Svoboda K and Kim D S 2013 Ultrasensitive fluorescent proteins for imaging neuronal activity Nature **499** 295–300

[21] Nakai J, Ohkura M and Imoto K 2001 A high signal-to-noise Ca2+ probe composed of a single green fluorescent protein Nat. Biotechnol. **19** 137–41

[22] Pastrana E 2013 Sensors and probes: Calcium sensors reach new heights Nat. Methods **10** 824–824

[23] Tian L, Hires S A, Mao T, Huber D, Chiappe M E, Chalasani S H, Petreanu L, Akerboom J, McKinney S A, Schreiter E R, Bargmann C I, Jayaraman V, Svoboda K and Looger L L 2009 Imaging neural activity in worms, flies and mice with improved GCaMP calcium indicators Nat. Methods **6** 875–81

[24] Antunes M, Pereira T, Cordeiro J V, Almeida L and Jacinto A 2013 Coordinated waves of actomyosin flow and apical cell constriction immediately after wounding J. Cell Biol. **202** 365–79

[25] Clapham D E 2007 Calcium signaling Cell **131** 1047–58

[26] Razzell W, Evans I R, Martin P and Wood W 2013 Calcium Flashes Orchestrate the Wound Inflammatory Response through DUOX Activation and Hydrogen Peroxide Release Curr. Biol. **23** 424–9

[27] Wood W 2012 Wound Healing: Calcium Flashes Illuminate Early Events Curr. Biol. **22** R14–6

[28] Razzell W, Wood W and Martin P 2014 Recapitulation of morphogenetic cell shape changes enables wound re-epithelialisation Development dev.107045

[29] Fain M J and Stevens B 1982 Alterations in the cell cycle of Drosophila imaginal disc cells precede metamorphosis Dev. Biol. **92** 247–58

[30] Garcia-Bellido A and Merriam J R 1971 Parameters of the wing imaginal disc development of Drosophila melanogaster Dev. Biol. **24** 61–87

[31] Restrepo S, Zartman J J and Basler K 2014 Coordination of patterning and growth by the morphogen DPP Curr. Biol. CB **24** R245–55

[32] Haynie J L and Bryant P J 1977 The effects of X-rays on the proliferation dynamics of cells in the imaginal wing disc ofDrosophila melanogaster Wilhelm Rouxs Arch. Dev. Biol. **183** 85–100

[33] Zartman J, Restrepo S and Basler K 2013 A high-throughput template for optimizing Drosophila organ culture with response-surface methods Dev. Camb. Engl. **140** 667–74

[34] Heemskerk I, Lecuit T and LeGoff L 2014 Dynamic clonal analysis based on chronic in vivo imaging allows multiscale quantification of growth in the Drosophila wing disc Dev. Camb. Engl. **141** 2339–48

[35] Sneyd J, Wetton B T, Charles A C and Sanderson M J 1995 Intercellular calcium waves mediated by diffusion of inositol trisphosphate: a two-dimensional model Am. J. Physiol. **268** C1537–45

[36] Höfer T, Venance L and Giaume C 2002 Control and Plasticity of Intercellular Calcium Waves in Astrocytes: A Modeling Approach J. Neurosci. **22** 4850–9

[37] Long J, Junkin M, Wong P K, Hoying J and Deymier P 2012 Calcium wave propagation in networks of endothelial cells: model-based theoretical and experimental study PLoS Comput. Biol. **8** e1002847

[38] Duffy J B 2002 GAL4 system in drosophila: A fly geneticist's swiss army knife genesis **34** 1–15

[39] Huang J, Zhou W, Dong W, Watson A M and Hong Y 2009 Directed, efficient, and versatile modifications of the Drosophila genome by genomic engineering Proc. Natl. Acad. Sci. pnas.0900641106

[40] Ashburner M 1989 Drosophila: A laboratory handbook (Cold Spring Harbor Laboratory)

[41] Xiao J, Liang D, Zhao H, Liu Y, Zhang H, Lu X, Liu Y, Li J, Peng L and Chen Y-H 2010 2-Aminoethoxydiphenyl borate, a inositol 1,4,5-triphosphate receptor inhibitor, prevents atrial fibrillation Exp. Biol. Med. Maywood NJ **235** 862–8

[42] Michelangeli F and East J M 2011 A diversity of SERCA Ca2+ pump inhibitors Biochem. Soc. Trans. **39** 789–97

[43] Diao H, Xiao S, Howerth E W, Zhao F, Li R, Ard M B and Ye X 2013 Broad gap junction blocker carbenoxolone disrupts uterine preparation for embryo implantation in mice Biol. Reprod. **89** 31

[44] Zhao F, Li P, Chen S R, Louis C F and Fruen B R 2001 Dantrolene inhibition of ryanodine receptor Ca2+ release channels. Molecular mechanism and isoform selectivity J. Biol. Chem. **276** 13810–6

[45] Ma J 1993 Block by ruthenium red of the ryanodine-activated calcium release channel of skeletal muscle J. Gen. Physiol. **102** 1031–56

[46] Kaneuchi T, Sartain C V, Takeo S, Horner V L, Buehner N A, Aigaki T and Wolfner M F 2015 Calcium waves occur as Drosophila oocytes activate Proc. Natl. Acad. Sci. **112** 791–6

[47] Schindelin J, Arganda-Carreras I, Frise E, Kaynig V, Longair M, Pietzsch T, Preibisch S, Rueden C, Saalfeld S, Schmid B, Tinevez J-Y, White D J, Hartenstein V, Eliceiri K, Tomancak P and Cardona A 2012 Fiji: an open-source platform for biological-image analysis Nat. Methods **9** 676–82

[48] Thévenaz P and Unser M 2007 User-friendly semiautomated assembly of accurate image mosaics in microscopy Microsc. Res. Tech. **70** 135–46

[49] Sezgin M and Sankur B 2004 Survey over image thresholding techniques and quantitative performance evaluation J. Electron. Imaging **13** 146–68

[50] Mashburn D N, Lynch H E, Ma X and Hutson M S 2012 Enabling user-guided segmentation and tracking of surface-labeled cells in time-lapse image sets of living tissues Cytometry A **81A** 409–18

[51] Falcke M 2004 Reading the patterns in living cells —the physics of ca $^{2+}$ signaling Adv. Phys. **53** 255–440

[52] Goldbeter A, Dupont G and Berridge M J 1990 Minimal model for signal-induced Ca2+ oscillations and for their frequency encoding through protein phosphorylation. Proc. Natl. Acad. Sci. **87** 1461–5

[53] MacLennan D H, Rice W J and Green N M 1997 The Mechanism of Ca2+ Transport by Sarco(Endo)plasmic Reticulum Ca2+-ATPases J. Biol. Chem. **272** 28815–8

[54] Stebbings L A, Todman M G, Phillips R, Greer C E, Tam J, Phelan P, Jacobs K, Bacon J P and Davies J A 2002 Gap junctions in Drosophila: developmental expression of the entire innexin gene family Mech. Dev. **113** 197–205

[55] Weir M P and Lo C W 1984 Gap-junctional communication compartments in the Drosophila wing imaginal disk Dev. Biol. **102** 130–46

[56] Parry H, McDougall A and Whitaker M 2005 Microdomains bounded by endoplasmic reticulum segregate cell cycle calcium transients in syncytial Drosophila embryos J. Cell Biol. **171** 47–59

[57] Agrawal N, Venkiteswaran G, Sadaf S, Padmanabhan N, Banerjee S and Hasan G 2010 Inositol 1,4,5-Trisphosphate Receptor and dSTIM Function in Drosophila Insulin-Producing Neurons Regulates Systemic Intracellular Calcium Homeostasis and Flight J. Neurosci. **30** 1301–13

[58] Banerjee S, Joshi R, Venkiteswaran G, Agrawal N, Srikanth S, Alam F and Hasan G 2006 Compensation of Inositol 1,4,5-Trisphosphate Receptor Function by Altering Sarco-Endoplasmic Reticulum Calcium ATPase Activity in the Drosophila Flight Circuit J. Neurosci. **26** 8278–88

[59] York-Andersen A H, Parton R M, Bi C J, Bromley C L, Davis I and Weil T T 2015 A single and rapid calcium wave at egg activation in Drosophila Biol. Open BIO201411296

[60] Raghu P and Hasan G 1995 The Inositol 1,4,5-Triphosphate Receptor Expression in Drosophila Suggests a Role for IP3 Signalling in Muscle Development and Adult Chemosensory Functions Dev. Biol. **171** 564–77

[61] Allbritton N L, Meyer T and Stryer L 1992 Range of messenger action of calcium ion and inositol 1,4,5-trisphosphate Science **258** 1812–5

[62] Sneyd J, Charles A C and Sanderson M J 1994 A model for the propagation of intercellular calcium waves Am. J. Physiol. **266** C293–302

[63] Taylor C W and Tovey S C 2010 IP3 Receptors: Toward Understanding Their Activation Cold Spring Harb. Perspect. Biol. **2** a004010

[64] Watson W D, Facchina S L, Grimaldi M and Verma A 2003 Sarco-endoplasmic reticulum Ca2+ ATPase (SERCA) inhibitors identify a novel calcium pool in the central nervous system J. Neurochem. **87** 30–43

[65] Pierce W G, Zanette C, Caplice N M and Mackrill J J 2012 Calcium signalling in adult endothelial outgrowth cells Biochem. Biophys. Res. Commun. **417** 358–63

[66] Nath S, Goodwin J, Engelborghs Y and Pountney D L 2011 Raised calcium promotes α-synuclein aggregate formation Mol. Cell. Neurosci. **46** 516–26

[67] Peracchia C 2004 Chemical gating of gap junction channels: Roles of calcium, pH and calmodulin Biochim. Biophys. Acta BBA - Biomembr. **1662** 61–80

[68] Berg J M, Tymoczko J L and Stryer L 2010 Biochemistry (W. H. Freeman)

[69] Lin M, Lucas H C and Shmueli G 2013 Research Commentary—Too Big to Fail: Large Samples and the p-Value Problem Inf. Syst. Res. **24** 906–17

[70] Mao Y, Tournier A L, Hoppe A, Kester L, Thompson B J and Tapon N 2013 Differential proliferation rates generate patterns of mechanical tension that orient tissue growth EMBO J. **32** 2790–803

[71] Legoff L, Rouault H and Lecuit T 2013 A global pattern of mechanical stress polarizes cell divisions and cell shape in the growing Drosophila wing disc Dev. Camb. Engl. **140** 4051–9

[72] Jaffe L F 2003 The propagation speeds of calcium action potentials are remarkably invariant Biol. Cell Auspices Eur. Cell Biol. Organ. **95** 343–55

[73] Shaw R M and Rudy Y 1997 Ionic Mechanisms of Propagation in Cardiac Tissue Roles of the Sodium and L-type Calcium Currents During Reduced Excitability and Decreased Gap Junction Coupling Circ. Res. **81** 727–41

[74] Allen M J, Gemel J, Beyer E C and Lal R 2011 Atomic Force Microscopy of Connexin40 Gap Junction Hemichannels Reveals Calcium-dependent Three-dimensional Molecular Topography and Open-Closed Conformations of Both the Extracellular and Cytoplasmic Faces J. Biol. Chem. **286** 22139–46

[75] Li Y, Naveed H, Kachalo S, Xu L X and Liang J 2012 Mechanisms of Regulating Cell Topology in Proliferating Epithelia: Impact of Division Plane, Mechanical Forces, and Cell Memory PLoS ONE **7** e43108

[76] Lynch H E, Veldhuis J, Brodland G W and Hutson M S 2014 Modeling cell elongation during germ band retraction: cell autonomy versus applied anisotropic stress New J. Phys. **16** 055003

[77] Schluck T and Aegerter C M 2010 Photo-elastic properties of the wing imaginal disc of Drosophila Eur. Phys. J. E Soft Matter **33** 111–5

[78] Nienhaus U, Aegerter-Wilmsen T and Aegerter C M 2009 Determination of mechanical stress distribution in Drosophila wing discs using photoelasticity Mech. Dev. **126** 942–9

[79] Li Y, Naveed H, Kachalo S, Xu L X and Liang J 2014 Mechanisms of Regulating Tissue Elongation in Drosophila Wing: Impact of Oriented Cell Divisions, Oriented Mechanical Forces, and Reduced Cell Size PLoS ONE **9** e86725

[80] Matakatsu H and Blair S S 2004 Interactions between Fat and Dachsous and the regulation of planar cell polarity in the Drosophila wing Development **131** 3785–94

[81] Kim D-H, Wong P K, Park J, Levchenko A and Sun Y 2009 Microengineered Platforms for Cell Mechanobiology Annu. Rev. Biomed. Eng. **11** 203–33

[82] Fletcher A G, Osterfield M, Baker R E and Shvartsman S Y 2014 Vertex models of epithelial morphogenesis Biophys. J. **106** 2291–304

[83] Smith A M, Baker R E, Kay D and Maini P K 2012 Incorporating chemical signalling factors into cell-based models of growing epithelial tissues J. Math. Biol. **65** 441–63

[84] El-Kholy W, Macdonald P E, Lin J-H, Wang J, Fox J M, Light P E, Wang Q, Tsushima R G and Wheeler M B 2003 The phosphatidylinositol 3-kinase inhibitor LY294002 potently blocks K(V) currents via a direct mechanism FASEB J. Off. Publ. Fed. Am. Soc. Exp. Biol. **17** 720–2

[85] Parys B, Côté A, Gallo V, De Koninck P and Sík A 2010 Intercellular calcium signaling between astrocytes and oligodendrocytes via gap junctions in culture Neuroscience **167** 1032–43

SUPPORTING MATERIAL

Supplementary Software

MATLAB code and Fiji macros used in data analysis are contained in the supplementary included file code.zip. See the contained README.txt for additional information on functionality.

Supplementary video 1: Central symmetric flash

The wing disc is obtained from a 3rd instar wandering larva expressing GCaMP6f ubiquitously. The flash was stimulated by point ablation with a UV laser in the center of the disc pouch. The flash expanded and receded symmetrically around the ablation center. The imaging interval was one second at 488nm excitation with a recording period of 109 seconds.

Supplementary video 2: Asymmetric flash

The wing disc is obtained from a 3rd instar wandering larva expressing GCaMP6f ubiquitously. The flash was stimulated by point ablation with a UV laser at the upper right edge of the disc pouch. The flash expanded and receded asymmetrically. The imaging interval was one second with a recording period of 287 seconds.

Supplementary Table S1: Summary of pharmacological results

Compound	Target	Concentration	Effect on flash response
2-APB	IP_3 receptor, [41,63]	200-400 μM	Severely reduced flash
LY294002	PI3K (production of IP_3) [84]	300 μM	Severely reduced flash
Carbenoxolone	Gap junctions, [85]	30-50 μM	Severely reduced flash
Thapsigargin	SERCA, [42,64]	30 μM	No effect
Ruthenium red	Ryanodine receptor, [45]	20 μM	No effect
Dantrolene	Ryanodine receptor, [44]	10 μM	No effect

TABLE S1 Summary of results for the effect of listed drugs on the Ca^{2+} response

Supplementary Figure S1: Extent of ablation

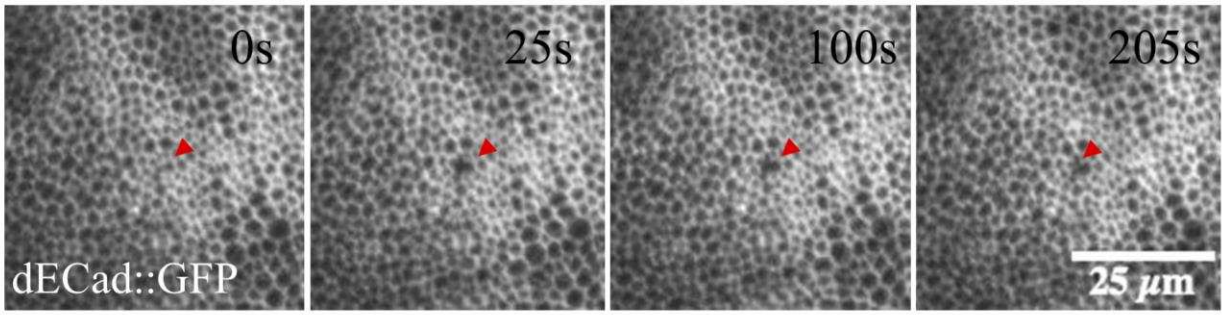

FIGURE S1 Extent of a typical ablation used in experiment is shown above. Cell boundaries are marked by dECadherin::GFP. Although the laser intensity used typically severs a single cell bond, heat and imperfect targeting of the ablation site may destroy neighboring cells in addition to the targeted cell. Each ablation destroys between 1 and 3 cells in the pouch to produce a small wound and subsequent Ca^{2+} flash.

Supplementary Figure S2: Error between cell-based and continuum model

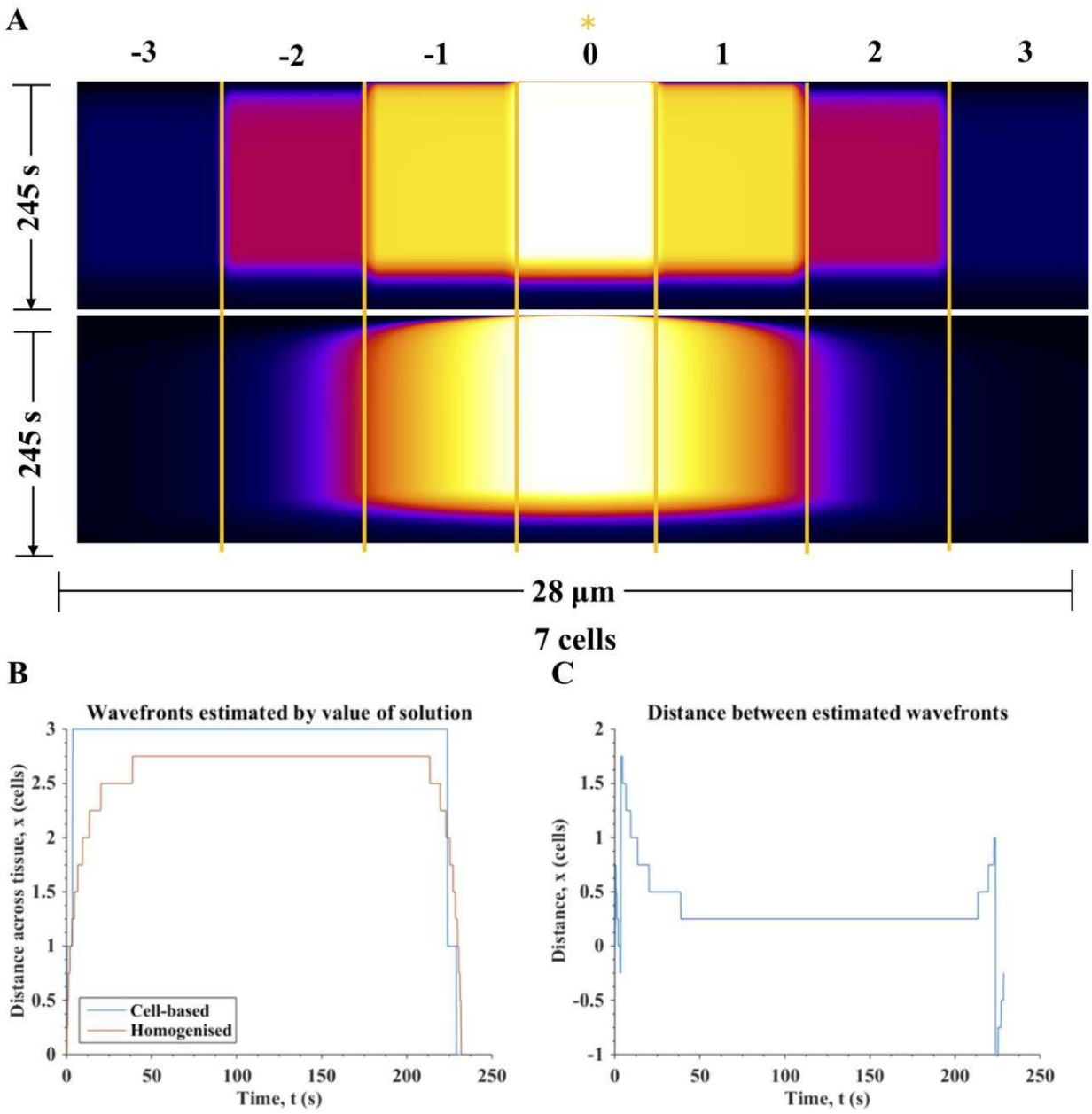

FIGURE S2 (A) Kymograph of 1D cell-based (upper) and continuum (lower) models simulated for 300 s. Locations of cell boundaries are marked by orange lines. Initially stimulated cell is marked by an orange asterisk. (B) Wavefronts estimated by thresholding of 1D solution for cell-based and continuum models. Cell-based is shown in blue, continuum in green. (C) Plot of the distance between cell-based and continuum model wavefronts demonstrating that the error between solutions is on the order of <1 cell diameter (<10%).

Supplementary Figure S3: Effect of ryanodine on the Ca^{2+} flash

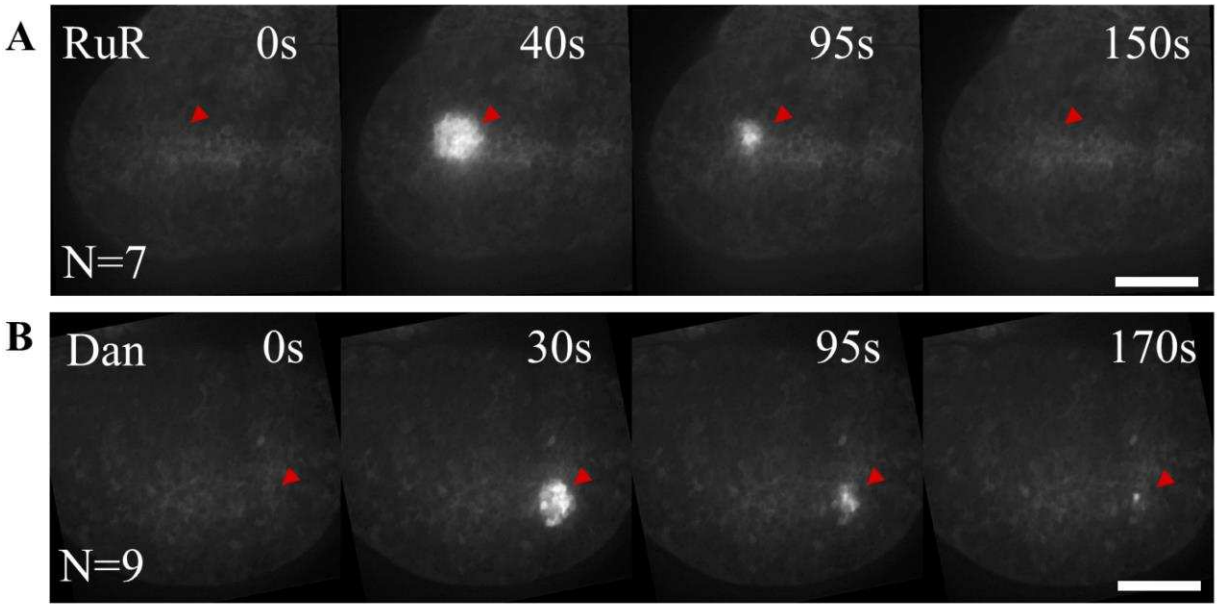

FIGURE S3 (A) Ablation in tissue incubated for one hour with 20 µM ruthenium red (RuR), a RyR inhibitor, shows normal flash propagation, demonstrating that the response is not a result of ryanodine mediated Ca2+ release. (B) Ablation in tissue incubated for one hour with 10 µM dantrolene, a RyR inhibitor shows normal flash propagation. All scale bars are 50 µm.

Supplemental Figure S4: Effects of abrupt cell changes

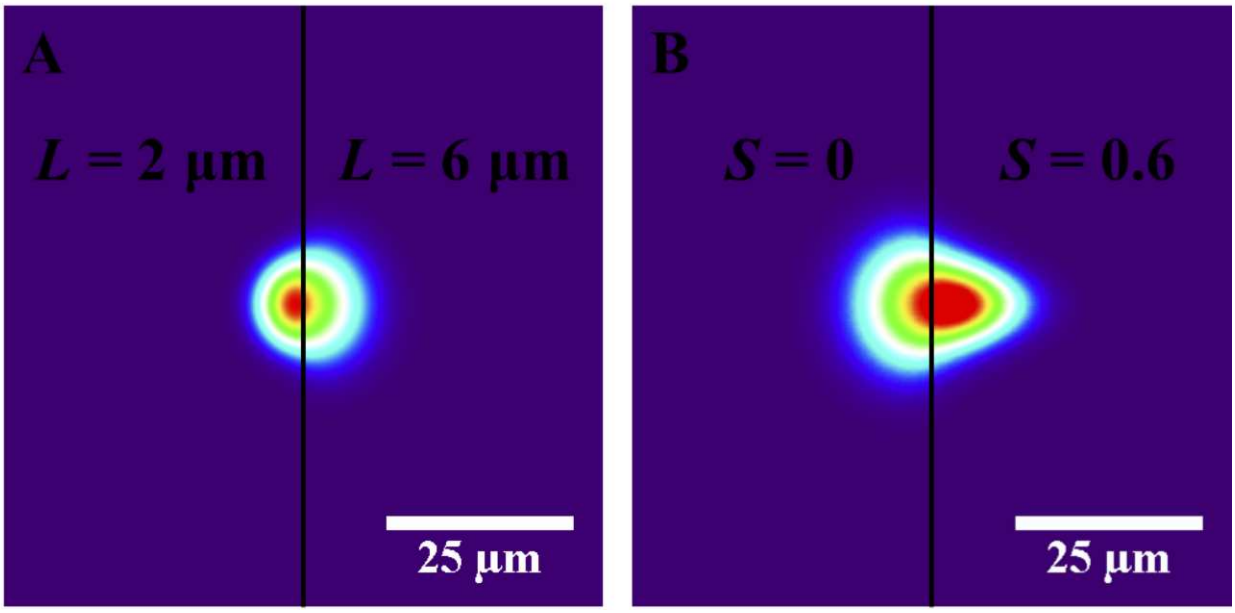

FIGURE S4 (A) An instantaneous jump in cell size produces no significant elongation of the Ca^{2+} transient. (B) An instantaneous jump in cell elongation produces elongated flashes consistent with experimental observations. Frames shown are from 60 s simulated time. In both cases stimulus is initiated at the center of the domain.

Supplementary Text

A sensitivity analysis was performed by individual parameter variation. Each parameter was separately increased and decreased 10% from the base value and the model output analyzed as described in the main text. The results are shown in (Fig. S1). We find that the model is most sensitive to changes in IP_3 degradation, V_P, and intercellular permeability of IP_3, α_P.

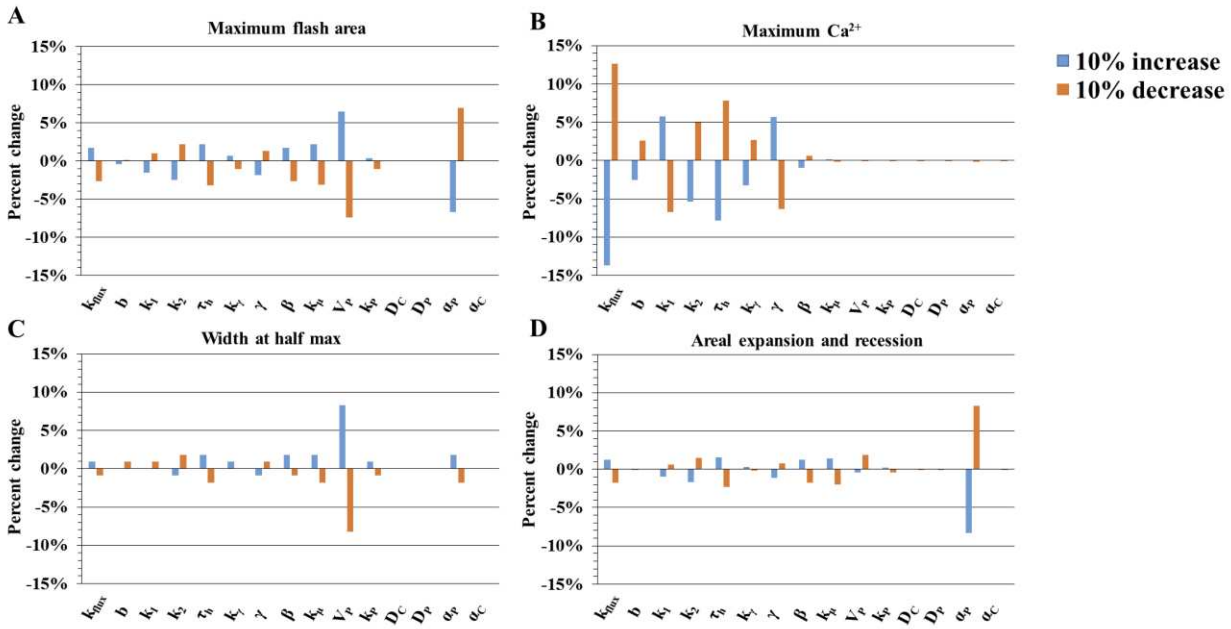

FIGURE S5 Model sensitivity. Blue bars represent percent change in the relevant metric as a result of a 10% increase to the parameter value. Orange bars represent the percent change as a result of a 10% decrease to the parameter value. **(A) Percent change in maximum flash area in response to parameter variation. (B) Percent change in maximum Ca^{2+} concentration in response to parameter variation. (C) Percent change in the width of the flash at half max area in response to parameter variation. (D) Percent change in areal expansion and recession in response to parameter variation.**